



HAL
open science

Germanium- and gallium-rich sphalerite in Mississippi Valley–type deposits: the San Vicente district and the Shalipayco deposit, Peru

Lisard Torró, Andrea Julieta Millán-Nuñez, Diego Benites, José María González-Jiménez, Oscar Laurent, Lorenzo Tavazzani, Jean Vallance, Cyril Chelle-Michou, Joaquín A Proenza, Carlos Flores, et al.

► To cite this version:

Lisard Torró, Andrea Julieta Millán-Nuñez, Diego Benites, José María González-Jiménez, Oscar Laurent, et al.. Germanium- and gallium-rich sphalerite in Mississippi Valley–type deposits: the San Vicente district and the Shalipayco deposit, Peru. *Mineralium Deposita*, 2023, 58 (5), pp.853 - 880. 10.1007/s00126-023-01160-4 . hal-04245404

HAL Id: hal-04245404

<https://hal.science/hal-04245404>

Submitted on 18 Oct 2023

HAL is a multi-disciplinary open access archive for the deposit and dissemination of scientific research documents, whether they are published or not. The documents may come from teaching and research institutions in France or abroad, or from public or private research centers.

L'archive ouverte pluridisciplinaire **HAL**, est destinée au dépôt et à la diffusion de documents scientifiques de niveau recherche, publiés ou non, émanant des établissements d'enseignement et de recherche français ou étrangers, des laboratoires publics ou privés.

1 **Germanium- and gallium-rich sphalerite in Mississippi Valley-type deposits: the San**
2 **Vicente district and the Shalipayco deposit, Peru**

3 Lisard Torró^{a,*}, Andrea J. Millán-Nuñez^a, Diego Benites^a, José María González-Jiménez^b,
4 Oscar Laurent^{c,**}, Lorenzo Tavazzani^c, Jean Vallance^a, Cyril Chelle-Michou^c, Joaquín A.
5 Proenza^d, Carlos Flores^e, Joan Carles Melgarejo^d, Silvia Rosas^a, Lluís Fontboté^f

6 ^a *Geological Engineering Program, Faculty of Sciences and Engineering, Pontifical Catholic*
7 *University of Peru (PUCP), Av. Universitaria 1801, San Miguel, Lima 15088, Peru*

8 ^b *Instituto Andaluz de Ciencias de la Tierra, CSIC-Universidad de Granada, Avda. de las*
9 *Palmeras 4, 18100 Armilla, Granada, Spain.*

10 ^c *ETH Zürich, Department of Earth Sciences, Institute for Geochemistry and Petrology,*
11 *Clausiusstrasse 25, 8092 Zürich, Switzerland*

12 ^d *Departament de Mineralogia, Petrologia i Geologia Aplicada, Facultat de Ciències de la*
13 *Terra, Universitat de Barcelona, Martí i Franquès s/n, 08028 Barcelona, Spain*

14 ^e *Compañía Minera San Ignacio de Morococha S.A.A.(SIMSA), Calle Manuel Gonzales*
15 *Olaechea 448, San Isidro, Lima 15047, Peru*

16 ^f *Department of Earth Sciences, University of Geneva, CH-1205 Geneva, Switzerland*

17 Submitted to *Mineralium Deposita*

18 *Corresponding author: Lisard Torró, lisardtorro@hotmail.com

19 Phone: (+51) 6262000 Ext. 5060

20 ** *Present address: CNRS, Géosciences Environnement Toulouse, Observatoire Midi-*
21 *Pyrénées, 31400 Toulouse, France*

22 **Abstract**

23 Sphalerite in Mississippi Valley-type (MVT) deposits hosts significant resources of both
24 germanium and gallium. Here, we provide a survey on the distribution of Ge, Ga, and other
25 minor and trace elements in sphalerite from MVT deposits in the Eastern Cordillera and Sub-
26 Andean regions of Peru, including the San Vicente deposit and the nearby Chilpes and
27 Huacrash prospects, and the Shalipayco deposit. We present also a micro- and nano-scale
28 textural characterization of Ge-rich sphalerite.

29 In situ LA-ICP-MS analyses yielded Ge contents (inter-quartile range [IQR] = 164-36 ppm for
30 the San Vicente district and IQR = 425-101 ppm for the Shalipayco deposit) that overlap with
31 the range reported for sphalerite from other MVT deposits elsewhere. The highest Ge
32 contents (IQR = 1,207-375 ppm, up to 1,861 ppm) were found in Fe-poor orange sphalerite
33 deposited during a volumetrically minor second mineralization step in the San Vicente deposit
34 located mainly in steep veins that cross-cut the main first-step mineralization dominated by
35 darker sphalerite. Reddish-brown sphalerite from Chilpes (IQR = 445-22 ppm, up to 1,745
36 ppm) and brownish orange sphalerite from Huacrash (IQR = 650-34 ppm, up to 855 ppm)
37 also yielded remarkably high Ge values. In Shalipayco, the highest Ge contents were
38 analyzed in late Fe-poor yellow sphalerite (IQR = 375-267 ppm, up to 1,119 ppm). The
39 highest Ga contents were determined in reddish-brown sphalerite from the Chilpes prospect
40 (IQR = 1,156-0.26 ppm, up to 3,943 ppm), although Ga contents are, in general, much lower
41 than those of Ge in most analyzed sphalerite (IQR = 27 – 0.22 ppm in the San Vicente district
42 and IQR = 2.8 – 0.081 ppm in the Shalipayco deposit). These figures place some of the
43 analyzed sphalerite types among the Ge- and Ga-richest samples ever reported.

44 Linkage of textural and compositional data points to light-colored, chiefly orange and yellow
45 sphalerite generations crystallizing at lower temperatures and relatively late in the paragenetic
46 sequences as those with the highest Ge contents. In contrast, the paragenetic control on Ga
47 enrichment is unclear. Focused ion beam and high-resolution transmission electron
48 microscopy (FIB-HRTEM) investigation combined with trace element content correlations
49 reveal selective partitioning of Ge and Ga into sphalerite as structurally-bound elements and
50 their incorporation via substitution mostly coupled to monovalent cations triggering
51 polytypism.

52 **Keywords:** Critical raw materials, high-tech elements, by-product, Zn-Pb deposits, Andes,
53 mineral color

54 **Introduction**

55 Germanium and gallium are considered critical raw materials by the [European Commission](#)
56 (2020) due to their high economic importance and risk of supply. Germanium is mainly used in
57 infrared optical devices, fiber-optic systems, photovoltaic cells, and as a catalyst in plastic
58 production ([Höll et al. 2007](#); [Melcher and Buchholz 2014](#); [Cook et al. 2015a](#)). Gallium is mainly
59 employed to manufacture optoelectronic devices (i.e., directly converting electricity into laser
60 light), integrated circuits, thin-film photovoltaic cells, and military technology (e.g., satellites,
61 radars, night vision equipment), as well as in the pharmaceutical industry for cancer treatment
62 ([Moskalyk 2003](#); [Foley et al. 2017](#)). Germanium and gallium are recovered as by-products of
63 zinc mining in sulfide deposits (e.g., Mississippi Valley-type [MVT], sedimentary-exhalative
64 [SEDEX], volcanogenic massive sulfides [VMS], or Kipushi-type deposits; [Foley et al. 2017](#),
65 [Shanks et al. 2017](#)). In addition, Ge is recovered from fly ash residues from coal burning and
66 Ga is a by-product in bauxite deposits ([Shanks et al. 2017](#); [Ujaczki et al. 2019](#)).

67 In sulfide deposits, Ge and Ga are mainly extracted from sphalerite, in which they are
68 incorporated under certain crystallization conditions and mostly via coupled substitutions
69 (Möller and Dulski 1996; Cook et al. 2009; Belissont et al. 2014; Cook et al. 2015a; Frenzel et
70 al. 2016; Liu et al. 2022; Luo et al. 2022). Sphalerite from MVT deposits is of particular interest
71 because it usually contains the highest Ge contents and, in general, is enriched in both Ge and
72 Ga in comparison to deposits of magmatic-hydrothermal origin (Bernstein 1985; Paradis 2015;
73 Frenzel et al. 2016; Shanks et al. 2017; Bauer et al. 2019; Wei et al. 2021; Benites et al. 2021,
74 2022). Background information on MVT deposits is available in Sangster (1995), Bradley and
75 Leach (2003), Leach et al. (2005, 2010), Wilkinson (2014), Ostendorf et al. (2015), and Saintilan
76 et al. (2019).

77 A MVT belt extends along the Eastern Cordillera and Sub-Andean Zone morphotectonic units
78 of central and northern Peru (Fig. 1). It includes the San Vicente, Shalipayco, and Florida
79 Canyon deposits, as well as dozens of inactive artisanal mines, prospects, and mineral
80 showings (Fontboté and Gorzawski 1990; Carlotto et al. 2009; Fontboté 2018; Mondillo et al.
81 2018a; de Oliveira et al. 2019, 2020; Chirico et al. 2022). The iconic San Vicente deposit is
82 operated by Compañía Minera San Ignacio de Morococha S.A.A. – SIMSA. From 1970 to 2019,
83 it produced more than 27 Mt ore grading 9.21 % Zn and 0.74 % Pb and as of 2021, the ore
84 reserves and indicated resources amount to 3.4 Mt grading 9.51 % Zn and 0.48 % Pb (SIMSA
85 2021). The Chilpes and Huacrash prospects in the San Vicente district (Fig. 2) were explored
86 in the 1990s by SIMSA through underground adits and diamond drilling and have yielded
87 several low-grade Zn-Pb, mostly manto, ore bodies. The Shalipayco Project, located 100 km
88 NE of San Vicente (Fig. 1), is a joint venture between Nexa Peru and Pan American Silver Peru
89 S.A.C. As of 2017, the Shalipayco deposit had total measured and indicated mineral resources

90 of 6.29 Mt grading 5.61 % Zn, 0.43 % Pb, and 38.5 g/t Ag, containing approximately 353,000 t
91 Zn, 27,000 t Pb, and 7.8 Moz Ag (Robson et al. 2017).

92 Further north (Fig. 1), and not studied in the present work, is the Bongará MVT district, which
93 includes the Florida Canyon deposit. Florida Canyon is under exploration by Nexa Peru and
94 has total measured and indicated resources of 2.4 Mt grading 10.6 % Zn, 1.3 % Pb, and 15 g/t
95 Ag and inferred resources of 14.8 Mt grading 9.6 % Zn, 1.3 % Pb, and 11.2 g/t Ag (Hulse et al.
96 2021). Samples of non-sulfide mineralization formed by supergene alteration of hypogene MVT
97 sulfide ore bodies in the Bongará district yielded Ge bulk contents up to 496 ppm (avg 162 ppm;
98 Chirico et al. 2022). In the same district, Mondillo et al. (2018b) also reported relatively high Ge
99 bulk values (up to 216 ppm) in samples of non-sulfide ore in the Cristal prospect, and Ga
100 contents of up to 27 ppm. Trace element determinations on precursor MVT sphalerite from this
101 deposit yielded average Ge contents of 142 ppm and average Ga contents of 1.3 ppm (Mondillo
102 et al. 2018b).

103 This work provides novel data on the minor and trace element contents of sphalerite from the
104 San Vicente district and the Shalipayco deposit in Peru acquired by means of LA-ICP-MS
105 analysis, focusing on Ge and Ga. Single-spot analysis guided by petrographic determinations
106 made it possible to recognize sphalerite types that are particularly enriched in Ge and Ga and
107 their position in the respective paragenetic sequences. The microanalytical work was
108 complemented by a combination of focused ion beam and high-resolution transmission electron
109 microscopy (FIB/HRTEM) that allowed observation of atomic-scale ordering of the different
110 sphalerite types, including those with Ge-rich domains. Additionally, the poorly understood
111 possible correlation between trace element contents and crystal color is explored in order to

112 develop practical tools for targeting Ge-rich sphalerite from early exploration stages in MVT
113 deposits.

114 **Geological setting**

115 *The MVT belt in Peru*

116 The MVT belt stretches along the Eastern Cordillera and Sub-Andean Zone morphotectonic
117 units of central and northern Peru. Mineralization is hosted by carbonate rocks of the NNW –
118 SSE trending Pucará Basin (Fig. 1; Benavides-Cáceres 1999; Rosas et al. 2007). The Pucará
119 Group, which in most studied places is more than 2,000 m thick, was deposited on top of
120 Paleozoic units and Triassic syn-rift volcanic and continental sedimentary rocks of the Mitu
121 Group in a wide carbonate platform during regional subsidence in Upper Triassic to Lower
122 Jurassic times (Noble et al. 1978; Kontak et al. 1985; Rosas et al. 2007; Spikings et al. 2016).
123 The Pucará Group extends for ~1,000 km in a NW – SE direction from central to northern Peru
124 and comprises, from base to top, the Chambará, Aramachay, and Condorsinga formations
125 (Szekely and Grose 1972; Mégard 1978; Loughman and Hallam 1982; Rosas et al. 2007). The
126 Norian-Rhaetian Chambará Formation is predominantly dolomitic, composed of a thick
127 sequence of dolostones interlayered with dolomitic, dark-gray, and fossiliferous limestones. In
128 the lower part of the sequence, a higher content of detrital material is observed; nodules of
129 chert are common (Rosas and Fontboté 1995). Shallow water carbonate deposits are abundant
130 and in parts include carbonate pseudomorphs after Ca-sulfates (Rosas et al. 2007). The upper
131 Rhaetian-Sinemurian Aramachay Formation is mostly formed by black argillaceous bituminous
132 limestones and black shales with high organic matter content (Szekely and Grose 1972; Rosas
133 et al. 2007). In the Western Cordillera of Central Peru, abundant material derived from siliceous
134 sponges typical of shallow platforms has been identified pointing out that, locally, the

135 Aramachay Formation does not record the typical transgression described by facies observed
136 along the Altiplano and Eastern Cordillera ([Ritterbush et al. 2015](#); [Rosas 2016](#)). The upper
137 Sinemurian-Toarcian Condorsinga Formation comprises packstone to grainstone limestone
138 with chert, dolomitic limestone with macrofossils, bioturbated limestone and, at its upper
139 portions, interbedded evaporite lenses ([Rosas and Fontboté 1995](#)). Compared to the
140 Chambará Formation, the Condorsinga Formation shows lower degrees of dolomitization and
141 less chert ([Rosas et al. 2007](#)).

142 Massive anhydrite/gypsum occur at the base of the Chambará Formation in different places,
143 including Morococha ([Stipetich et al. 2022](#)), Ayawilca, ([Benites et al. 2022](#); [Ramírez et al. 2022](#)),
144 and at San Vicente, interbedded with red sandstone ([Fontboté and Gorzawski 1990](#); [Moritz et](#)
145 [al. 1996](#)). Evaporite beds occur also in other stratigraphic positions within the Pucará Group
146 ([Rosas et al. 2007](#)) and in time-equivalent units in the Amazonian foreland of Peru ([Carrillo et](#)
147 [al. 2022](#)). Evidence of salt tectonics have been described by [Berrospi-Rodriguez et al. \(2018\)](#),
148 [Sempere and Cotrina \(2018\)](#), [de Oliveira et al. \(2019, 2020\)](#), and [Benites et al. \(2022\)](#). Sporadic
149 andesitic-basaltic flows and local tuffaceous layers occur at different stratigraphic positions in
150 the Pucará column ([Muñoz et al. 2000](#); [Rosas et al. 2007](#); [Schaltegger et al. 2008](#)).

151 Reactivation of pre-Andean, steeply dipping NW – SE and NE – SW striking fractures resulted
152 in the formation of horsts and grabens that controlled the facies of the Pucará Group sediments
153 and could also act as feeders during mineralization. MVT mineralization along the belt was most
154 probably synchronous with first overthrusting in the Sub-Andean region ([Dávila et al. 2000](#);
155 [Badoux et al. 2001](#)), which occurred as early as in Upper Cretaceous – Paleocene times
156 according to [Baby et al. \(2019\)](#), during the Peruvian episode of the Andean orogeny (see
157 [Benavides-Cáceres 1999](#)). This time constraint of the mineralization based on structural

158 features in the San Vicente deposit accords well with Rb-Sr dates on sphalerite from the Florida
159 Canyon MVT deposit at ca. 86-83 Ma ([de Oliveira et al. 2020](#)).

160 *The San Vicente deposit and the Chilpes and Huacrash prospects*

161 The San Vicente MVT district is located ~300 km east of Lima at an altitude between 1,200 and
162 2,500 m.a.s.l. in the Sub-Andean Zone, at the limit with the Eastern Cordillera. It includes the
163 San Vicente deposit (11°14'S, 75°22'W) and several prospects such as Puntayacu Junior,
164 Palmapata, Quebrada Seca, Chilpes, Huacrash, Sillapata, and Piñón, all of them hosted by
165 dolomitic rocks of the Pucará Group ([Figs. 1, 2](#)).

166 As in other parts of the Sub-Andean region, the San Vicente area was affected by Upper
167 Cretaceous and Tertiary thin-skinned tectonics with numerous low-angle N – S to NNW – SSE
168 striking faults with E-vergence ([Fig. 2](#); [Fontboté and Gorzawski 1990](#); [Dávila et al. 2000](#)). In
169 addition, regional steep NW – SE and SW – NE striking faults cross-cut the rock sequence in
170 the area. The oldest rocks occur in the western part of the study area as a major tectonic slice
171 of the pre-Devonian ([Chew et al. 2016](#)) Maraynioc metamorphic complex thrust on top of
172 younger rocks ([Fig. 2](#)). The Maraynioc metamorphic complex is composed of deformed
173 micaschist, amphibolite, and gneiss cut by Carboniferous intrusive rocks ([Chew et al. 2016](#)).
174 More to the east and in the footwall of this major overthrust occurs the Carboniferous Utcuyacu
175 Granite (U-Pb zircon date of 307.05 ± 0.65 Ma on a sample collected 8 km NW of San Vicente,
176 at the road between Tarma and San Ramón; [Chew et al. 2007](#)) that, in turn, was thrust on top
177 of Pucará Group rocks. In the San Vicente mine, [Gunnesch et al. \(1990\)](#) dated the so-called
178 "Tarma granite", which is also thrust on the Pucará sequence, at 240 ± 4 Ma. As explained by
179 [Fontboté and Gorwaski \(1990\)](#), in the mine reports the terms Utcuyacu granodiorite and "Tarma

180 Grey Granite" are used indistinctly although the quoted dates suggest that rocks of different
181 ages are included under both terms.

182 Phyllites of the Excelsior Group, of probable Devonian age (McLaughlin 1924; Jenks 1951;
183 Saintilan et al. 2021), underlying the Mitu Group have been recognized ~15 km southeast of
184 the San Vicente mine (Fig. 2; Dávila et al. 2000). Sedimentary rocks of the Pennsylvanian-Early
185 Permian Tarma-Copacabana Group, including limestone and subordinate sandstone, black
186 shale, and cherty limestone (Wood et al. 2002), occur to the east and southeast of San Vicente
187 (Fig. 2). The Lower Triassic San Ramon Granite, dated at 246 ± 10 Ma (Capdevila et al. 1977;
188 recalculated by Lancelot et al. 1978) and at 255 ± 1 Ma (Gunnesch et al. 1990), occurs east of
189 San Vicente (Fig. 2).

190 In the central part of the San Vicente deposit, the three formations constituting the Pucará
191 Group have a total thickness of 1,400 m (Fontboté and Gorzawski 1990). The Chambará
192 Formation is 1,200 m thick and includes two main ore-bearing dolomitic units known as the San
193 Judas Dolomite (~280 m thick) and the – by far economically more important – San Vicente
194 Dolomite (~ 300 m thick; Fontboté and Gorzawski 1990; Spangenberg et al. 1996, 1999). Both
195 units consist mainly of dolomitized barrier calc-arenite (oolitic packstone to grainstone)
196 intercalated with very fine- to fine-grained dolomite deposited in lagoon and tidal flat
197 environments with fairly abundant evaporite pseudomorphs (Rosas et al. 2007). Massive
198 anhydrite layers occur at the bottom of the Chambará Formation intercalated with red
199 sandstone. The Aramachay Formation is represented in San Vicente by the Uncush bituminous
200 limestone (8 to 250 m thick), a hydrocarbon-source rock characterized by its high organic matter
201 content and pyrite dissemination that acted as a main seal during the mineralization process
202 atop the San Vicente unit (Dávila et al. 2000; Spangenberg et al. 1996, 1999). Mapping of the

203 strong thickness variations (8 to 250 m) of the Aramachay Formation indicates that at least part
204 of the NNW – SSE steep faults were active during sedimentation. The overlying Condorsinga
205 Formation (~120 m thick, top cut by overthrust faults) includes a third ore-bearing dolomitic unit,
206 the Alfonso Dolomite, which has similar characteristics as the San Judas and San Vicente
207 dolomitic units.

208 Orebodies of the San Vicente mine are mostly lens-shaped and tend to be parallel to the
209 bedding and to the low-angle overthrust planes, mainly in the upper portion of the central and
210 northern part of the deposit ([Fontboté and Gorzawski 1990](#)). In addition, the orebodies are
211 limited by steep NWW – SEE striking fractures, particularly in the deeper and southern parts of
212 the deposit ([Dávila et al. 2000, 2014](#)). Both the low-angle thrust faults and the steep NWW –
213 SEE trending fractures are interpreted to have acted as feeders of the metal-bearing fluids.

214 Ore minerals are essentially dark to light brown sphalerite and subordinate galena, with traces
215 of pyrite, marcasite, chalcopyrite, and sulfosalts. The gangue is mainly constituted by
216 hydrothermal dolomite, ranging from fine- to coarse-grained and including white sparry dolomite
217 (WSD), and minor calcite. In addition to disseminated organic matter in dolomite, massive
218 bitumen is present along faults and coating WSD. In the upper, northern part of the deposit,
219 lenticular bodies of massive pyrite pseudomorphic after marcasite occur. A significant portion
220 of the ore shows zebra (cf. [Fontboté 1993](#); [Leach et al. 2005](#); [Merino and Canals 2011](#); [Kelka
221 et al. 2017](#)), breccia, and vein textures and structures. Zebra, vein, and breccia fabrics occur
222 also abundantly in barren parts of the ore-bearing units with similar textures ([Fontboté and
223 Gorzawski 1990](#); [Fontboté et al. 1995](#); [Spangenberg 1995](#); [Badoux et al. 2001](#)). Volumetrically
224 minor Fe-poor orange and yellow sphalerite is found in steep veins that cross-cut the main

225 mineralization and belongs to a minor second mineralization step in the San Vicente deposit
226 that, as explained below, has a particular geochemical signature.

227 Ore formation is interpreted to have resulted mostly from the ingression of metal-bearing
228 basinal brines that encountered H₂S formed by thermochemical sulfate reduction (TSR) in
229 hydrocarbon traps located in dolomitized oolitic bars ([Fontboté and Gorzawski 1990](#), [Fontboté
230 et al. 1995](#); [Spangenberg 1995](#); [Spangenberg and Macko 1998](#); [Spangenberg et al. 1999](#)).
231 Lead and strontium isotope compositions of ore and host rocks suggest that the brines
232 scavenged metals from basement rocks. TSR as the main process for sulfur reduction is
233 indicated by the sphalerite and galena sulfur isotope composition close to that of Triassic
234 evaporites, the study of hydrocarbons occurring in ore and host rocks, and the very light carbon
235 isotope signatures – typical of organic carbon – measured in certain hydrothermal carbonate
236 generations of San Vicente. Exploratory fluid inclusion microthermometry on sparry dolomite
237 yielded homogenization temperatures in the range between 115 and 162°C and salinities
238 between 9.5 wt% and 26 wt% NaCl equivalent ([Moritz et al. 1996](#)). This temperature range is
239 compatible with sulfur isotope sphalerite-galena geothermometry reported by [Schuffert \(2001\)](#).

240 The Chilpes (11°15'S, 75°22'W) and Huacrash (11°16'S, 75°22'W) prospects are located
241 approximately 7 km and 8 km to the SSE of the San Vicente deposit, respectively ([Fig. 2](#)). At
242 both sites, low-grade Zn-Pb mineralization occurs in the Chambará Formation. Mineralization
243 at Chilpes is hosted by the San Judas dolomite and comprises sphalerite and galena
244 dissemination in coarsely crystalline dolomite with relictic oolitic grainstone texture; two massive
245 pyrite bands a few centimeters in thickness within fault planes are described by [Fontboté and
246 Gorzawski \(1990\)](#) as a distinctive feature at Chilpes. At Huacrash, an ~60 m-thick portion of the
247 San Vicente dolomite contains irregular ore lenses with sphalerite, galena, and coarse-grained

248 sparry dolomite. Centimetric patches of massive pyrite occur too and bitumen coats joints and
249 voids.

250 A Pb isotope study on sulfide minerals (sphalerite, galena, pyrite, and marcasite) from the San
251 Vicente deposit and the Chilpes and Huacrash prospects has been recently performed ([Bastian](#)
252 [2021](#); written communication of Lena Bastian, ETHZ). The results indicate that sulfides that
253 crystallized during the volumetrically dominant first mineralization step in the San Vicente
254 deposit are more radiogenic than sulfides in the Chilpes and Huacrash prospects, as well as
255 sulfides crystallized during the volumetrically much restricted second mineralization step at the
256 San Vicente deposit.

257 *The Shalipayco deposit*

258 The Shalipayco deposit (10°51'S, 75°58'W) is located ~170 km northeast of Lima in the central
259 Eastern Cordillera of Peru at an altitude of 4,400 m.a.s.l. ([Fig. 1](#)). An unconformity separates
260 the Chambará Formation from the underlying Mitu Group ([de Oliveira et al. 2019](#)). The ore-
261 hosting Pucará Group carbonate rocks in the Shalipayco area are moderately folded, occurring
262 at the deposit site as a monocline dipping between 30° and 45° to the southwest ([Robson et al.](#)
263 [2017](#)). The NW – SE oriented Ulcumayo-San Rafael thrust fault separates the Mitu Group from
264 the underlying Pucará Group, and the Yanacocha-Quilcatacta thrust fault, also NW – SE
265 striking, is within limestone of the Condorsinga Formation ([Robson et al. 2017](#)). Steeply dipping
266 N – S to NW – SW striking faults, including Eddy, San Teodoro, Virgencita, Pucará, and Santa
267 Inés could have served as feeder channels for mineralization ([Robson et al. 2017](#); [de Oliveira](#)
268 [et al. 2021](#)). Geologic maps showing the geology of the Shalipayco deposit are available in
269 Figures 1 and 2 in [de Oliveira et al. \(2021\)](#).

270 [De Oliveira et al. \(2021\)](#) divided the Chambará Formation, host of the mineralization in
271 Shalipayco, into four members which, from base to top, are i) the ~320 m-thick Chambará I
272 Member, which is mainly formed by dark-gray lime mudstone to wackestone with chert clasts
273 and calcite as cavity-filling and veins; ii) the ~120 m-thick Chambará II Member, which
274 essentially constitutes porous gray dolostone (wackestone) with local mudstone; iii) the ~80 m-
275 thick Chambará III Member, which is composed of beige dolomite boundstone with evaporitic
276 rocks and calcite veins; and iv) the ~130 m-thick Chambará IV Member, which is composed of
277 light gray mudstone with local dolomitization.

278 The stratabound – at the outcrop scale – and mostly stratiform orebodies in Shalipayco, namely
279 Intermedios and Resurgidora, are largely hosted by the Chambará II and III members,
280 respectively ([Robson et al. 2017](#); [de Oliveira et al. 2020, 2021](#)). The Intermedios level has an
281 average thickness of 8 m (up to 25 m) and extends for at least 2 km along strike ([de Oliveira et](#)
282 [al. 2021](#)). It is located above dark gray mudstone and wackestone and below dark gray sparry
283 fetid dolomite rich in organic matter ([Oldham et al. 2017](#)). Approximately 45% of the Zn-Pb
284 mineralization occurs along this horizon and is mainly hosted by porous coarse-grained
285 dolostone. The Resurgidora level has an average thickness of 4 m (up to 11 m) and extends
286 for at least 4 km along strike ([de Oliveira et al. 2021](#)). It is located between two horizons of
287 coarse-grained, dark, fetid dolomite rich in organic matter ([Oldham et al. 2017](#)) and is mainly
288 hosted by coarse-grained dolostone and evaporitic breccia ([de Oliveira et al. 2021](#)). Vein
289 mineralization is mainly represented by the Eddy vein (up to 8 m thick), currently considered as
290 one of the potential feeders ([Robson et al. 2017](#); [de Oliveira et al. 2021](#)). The main ore minerals
291 are sphalerite and galena with lesser amounts of pyrite, marcasite, and Ag sulfosalts ([Moritz et](#)
292 [al. 1996](#); [Oldham et al. 2017](#)). The main gangue minerals are dolomite, calcite, quartz, and
293 barite.

294 Strontium isotope signatures evolve from values typical of Norian seawater in least-altered
295 limestone to increasingly more radiogenic values in diagenetic replacement dolomite and ore-
296 intergrown dolomite and calcite, thus suggesting enhanced interaction with hydrothermal fluids
297 that circulated through basement rocks with radiogenic Sr (Moritz et al. 1996; de Oliveira et al.
298 2021). As in San Vicente, C and O isotope values of carbonates from Shalipayco also show a
299 progression from signatures that match the $\delta^{13}\text{C}$ and $\delta^{18}\text{O}$ of Triassic marine limestones to
300 isotopically lighter signatures along the aforementioned carbonate sequence (Moritz et al. 1996;
301 de Oliveira et al. 2021). Light $\delta^{34}\text{S}$ values in sulfides from Shalipayco led de Oliveira et al. (2021)
302 to propose that reduced sulfur mainly originated from bacteriogenic sulfate reduction and that,
303 in addition, evaporitic sulfate subsequently underwent thermochemical reduction by
304 bacteriogenic H_2S .

305 **Sampling and analytical methods**

306 *Sampling and petrography*

307 Sampling was focused on sphalerite of different color and/or textural features, ideally enabling
308 to establish a paragenetic sequence. A total of 36 sphalerite-rich ore samples were collected
309 from the San Vicente deposit (n = 16) and the Chilpes (n = 3) and Huacrash (n = 1) prospects
310 in the San Vicente district, and from the Shalipayco deposit (n = 16). In the San Vicente deposit,
311 sampling was conducted on drillholes (n = 14) and mine adits (n = 2) in the central (Ayala Inferior
312 manto) and the northernmost (Orcopunco) parts of the deposit. Samples from Chilpes and
313 Huacrash were taken from prospection adits. In Shalipayco, all samples were picked from
314 drillcore and come from the Resurgidora and Intermedio levels. Location including name/label
315 of the sampled mine adits and drillholes, and the mineralogy and hand sample textures are
316 given in [Table S1](#) in the [Electronic Supplementary Material](#). A total of 44 thick polished sections

317 were prepared at the QEMSCAN laboratory of the Pontifical Catholic University of Peru (PUCP)
318 for study under the optical microscope using reflected light. A selection of 5 samples was
319 examined on a Tescan VEGA II XMU SEM with a BRUKER xFlash 6/30 EDS microanalysis
320 system at BIZALab S.A.C., Lima. The operating conditions were 20 kV accelerating voltage and
321 105 μ A in backscattered electron (BSE) imaging mode.

322 *Electron microprobe analysis (EMPA)*

323 Mineral chemical analyses of sphalerite from San Vicente were performed using a five-channel
324 JEOL JXA-8230 electron microprobe at Centres Científics i Tecnològics of the University of
325 Barcelona (CCiT-UB). The instrument was operated at 20 kV acceleration voltage, 20 nA beam
326 current, and with a beam diameter of 5 μ m. Analytical standards and emission lines used for
327 analyses were as follows: sphalerite (Zn and S, $K\alpha$), chalcopyrite (Cu, $K\alpha$), FeS_2 (Fe, $K\alpha$), PbS
328 (Pb, $M\alpha$), CdS (Cd, $L\beta$), GaAs (As, $L\beta$; Ga, $K\alpha$), In_2Se (In, $L\beta$), Ag (Ag, $L\alpha$), Sb (Sb, $L\alpha$), Sn
329 (Sn, $L\alpha$), and Ge (Ge, $K\alpha$). The detection limits (d.l.) for each element and representative
330 analyses (values in wt% and atoms per formula unit - a.p.f.u.) are given in [Table S2](#) in
331 [Supplementary Material](#). Sphalerite compositions were normalized to 1 S.

332 *Laser ablation-inductively coupled plasma-mass spectrometry (LA-ICP-MS)*

333 Analyses of sphalerite trace element content were carried out at ETH Zürich, Switzerland, by
334 laser ablation-inductively coupled plasma-sector field-mass spectrometry (LA-ICP-SF-MS)
335 using a RESOLution S-155 (ASI/Applied Spectra) 193 nm ArF excimer laser system attached to
336 an Element XR (Thermo) sector-field ICP-MS. We used a laser repetition rate of 3 Hz, a spot
337 diameter of 19 μ m, and a laser energy density of ca. 2.5 $J\cdot cm^{-2}$. The sample surface was
338 cleaned before each analysis by three pre-ablation pulses. Ablation was performed in a dual-

339 volume, fast-washout S-155 ablation cell (Laurin Technic) fluxed with carrier gas consisting of
340 ca. 0.5 l·min⁻¹ He and make-up gas consisting of ca. 1 l·min⁻¹ Ar and 2 ml·min⁻¹ N₂. The ablated
341 aerosol was homogenized via flushing through an in-house built squid device before being
342 introduced in the plasma.

343 The ICP-MS instrument is equipped with a high capacity (80 m³·h⁻¹) interface pump to achieve,
344 in combination with jet sampler and normal H-skimmer cones, a detection efficiency (based on
345 U in NIST-SRM612 glass) in the range of 2% (Guillong et al. 2020). The instrument was
346 optimized for maximum sensitivity on the entire mass range while keeping low the production
347 of oxides (²⁴⁸ThO⁺/²³²Th⁺ ≤0.15%) and the U/Th ratio at ca. 1 (on NIST SRM612 glass). The list
348 of analyzed isotopes and corresponding dwell times is provided in Table S3 in the Electronic
349 Supplementary Material. A total of 68 mass scans (ca. 0.72 s sweep time each) were acquired
350 over ca. 50 s measurement (25 s of background measurement followed by 25 s of sample
351 ablation).

352 The resulting intensities were subsequently processed offline with the stand-alone version 1.3.2
353 of the SILLS program (Guillong et al. 2008) and the version 4.5 of the Lolite v4.5 software (Paton
354 et al. 2011). The pressed pellet MASS-1 sulfide standard (former PS-1; Wilson et al. 2002) was
355 used as the primary reference material for trace element quantification and instrumental drift
356 correction using conventional standard-sample bracketing. The Zn contents obtained by EMPA
357 for sphalerite from the San Vicente deposit were used as internal standard for relative sensitivity
358 corrections. For sphalerite from Chilpes, Huacrash, and Shalipayco, which are Fe-poor,
359 stoichiometric Zn was used as internal standard. The analyzed In intensities on masses 113
360 and 115, respectively, were corrected for polybaric interferences by subtracting the contribution
361 of ¹¹³Cd and ¹¹⁵Sn, respectively, based on the measured ¹¹¹Cd and ¹¹⁸Sn intensities and using

362 natural isotope ratios for Cd and Sn recommended by IUPAC. Because of the very high ^{111}Cd
363 signal (>10000 cps), the extent of the correction is much higher in the case of ^{115}In than in the
364 case of ^{113}In , especially because the analyzed sphalerite crystals all show relatively low Sn
365 contents (<100 ppm). Therefore, we considered only the contents based on the interference-
366 corrected ^{115}In intensities. The data are reported in Table S4 in the Electronic Supplementary
367 Material; a summary of the obtained minor and trace element contents is reported in Table 1.

368 The analytical reproducibility was checked by repeated measurements of the GSD-1G (Guillong
369 et al. 2005) and NIST-SRM610 (Jochum et al. 2011) glass reference materials, and ranges from
370 10 to 30% relative (2σ) for most elements. The quoted uncertainties for each analysis
371 correspond to the internal (2σ) statistical error and analytical reproducibility propagated by
372 quadratic addition. Accuracy was controlled by repeated measurements of the pressed pellet
373 UQAC-FeS-1 sulfide standard (unpublished data from D. Savard, UQAC, 2018; see also
374 Baumgartner et al. 2020). The results (reported in Table S4 in the Electronic Supplementary
375 Material) show that the measurements are accurate within the calculated uncertainties.

376 *High-resolution transmission electron microscopy (HRTEM)*

377 The HRTEM study was done on four thin foils of sphalerite from the San Vicente deposit. Two
378 thin foils cover contacts between white (sl_{2w} in the classification scheme explained in the
379 “Mineralogy and textures” section below) and black (sl_{1bl}) and between white (sl_{2w}) and yellow
380 (sl_{2y}) sphalerite types, while the other two thin foils are from the inner portion of yellow (sl_{2y})
381 and orange (sl_{2o}) sphalerites types. The thin foils were prepared and extracted by using a
382 focused ion beam-scanning electron microscope (FIB-SEM) in the Laboratorio de
383 Microscopías Avanzadas (LMA) at the Instituto de Nanociencia de Aragón (INA) – University
384 of Zaragoza, Spain. The TEM thin foil preparation was performed using a Dual Beam FEI

385 Thermo-Fisher Scientific, model Helios 650. The selected regions of interest were first
386 covered by a thin carbon strip (~300 nm) by focused electron beam induced deposition
387 (FEBID) and subsequently with a second strip (~1 μm) of Pt. These strips act as protection
388 during the milling, polishing, and extraction process of the thin foils. The bulk material was
389 first removed on both sides of the lamella by rough Ga^+ ion milling with a 30 kV current at 2.5
390 nA and the subsequent polishing with a 30 kV current at 0.23 nA. The final polishing step was
391 performed on the sample until electron transparency was achieved. This was completed by
392 subsequently milling the thin foil with a 5 kV current at 68 pA. The electron transparency was
393 monitored by an Everhart-Thornley SE detector using a 5 kV electron beam. After achieving
394 the electron transparency, the thin foil was rapidly polished using a low energy 5 kV current at
395 10 pA to reduce amorphization until a final thin foil thickness of ~90 nm was attained.
396 Subsequently, the thin foil was undercut with a 30 kV at 2.5 nA current, lifted out, and
397 transferred from the sample to a TEM grid using an OmniProbe nano-manipulator with a
398 tungsten tip. To weld the thin foil to the tungsten tip and the TEM grid, ion-beam assisted Pt
399 deposition was performed.

400 A FEI Titan G2 transmission electron microscope (TEM) equipped with a field emission gun
401 XFEG was used to analyze the thin foils at the Centro de Instrumentation Científica of the
402 University of Granada, Spain. The FEI Titan G2 microscope is equipped with four energy
403 dispersive X-ray (EDX) detectors (FEI microanalysis Super X) and a high-angle annular dark-
404 field detector (HAADF). This FEI Titan G2 microscope also includes a spherical correction for
405 the objective lens. Selected mineral areas of samples of interest within the thin foils were
406 imaged by the FEI Titan G2 microscope using a combination of high-angle annular dark-field
407 (HAADF) to obtain good Z-contrast images, and high-resolution transmission electron (HRTEM)
408 images to characterize the texture of the grains and to properly define the ordering of the

409 mineral aggregates. All these images were treated using the Digital Micrograph® software
410 (version 1.71.38) while maps were processed with the VELOX® software package. The FEI
411 Titan G2 run at 300 kV working conditions while HRTEM images were acquired using a Gatan
412 CCD Camera. Single-spot and elemental maps were also processed using the VELOX®
413 software.

414 **Mineralogy and textures**

415 *San Vicente district*

416 The studied samples from the San Vicente district are mainly composed of sphalerite with lesser
417 proportions of galena, pyrite, marcasite, and gratonite [Pb₉As₄S₁₅]. Hydrothermal dolomite is
418 the main gangue mineral, whereas hydrothermal calcite and quartz are locally present.

419 The main textures include the following: a) zebra-type, with up to 1 cm-wide dark bands of fine-
420 to medium-grained dolomite and sphalerite overgrown by up to 2 cm-wide bands of sparry
421 dolomite ± sphalerite and galena displaying a more or less rhythmical pattern (Fig. 3A); b)
422 colloform banding of sphalerite and dolomite (Figs. 3B-E); c) breccias with clasts constituted
423 mainly of fine- to medium-grained dolomite ± sphalerite cemented by white sparry dolomite
424 (WSD; Fig. 3F); and d) replacement between different types of sphalerite and hydrothermal
425 carbonates (Figs. 3G-I). Textures shown in Fig. 3C indicate significant dissolution between
426 precipitation of sphalerite and white sparry dolomite 1 yielding a breccia-like appearance not
427 caused by fracturing but by corrosion.

428 Three generations of hydrothermal dolomite have been recognized in the studied samples: dark
429 replacement dolomite (DRD), white sparry dolomite 1 (WSD₁), and white sparry dolomite 2
430 (WSD₂), the latter two formed mainly as open space-filling. Hydrothermal calcite appears as

431 thin veins across and filling spaces within WSD and is generally younger than dolomite (see
432 also textural descriptions in [Spangenberg et al. 1999](#)). Dark replacement dolomite is very-fine
433 to medium-grained, and in many places shows inclusions of fine-grained pyrite, organic matter,
434 and quartz.

435 In general, sphalerite grains at San Vicente are between ~25 μm and <1 mm in size, and are
436 mostly devoid of visible mineral inclusions, except for local dissemination of pyrite/marcasite
437 ([Figs. 4A-C](#)). Up to seven types of sphalerite have been differentiated according to their color
438 (including the color of internal reflections under the petrographic microscope) and textural
439 relationships. These sphalerite types have been ascribed to the two aforementioned
440 mineralizing episodes or “steps”. Sphalerite formed during the first mineralization step (sl_1)
441 accounts for most of the San Vicente ore and includes the black (sl_{1bl}), reddish-brown (sl_{1rb}),
442 yellowish-brown (sl_{1yb}), and yellow (sl_{1y}) types. Black sphalerite (sl_{1bl}) occurs mostly in the
443 central part of sphalerite zebra bands where it is followed from the inside outwards by reddish-
444 brown (sl_{1rb}) and yellowish-brown (sl_{1yb}) sphalerite bands ([Figs. 3A](#)). Black sphalerite (sl_{1bl}) is
445 also found replacing DRD without zebra fabric, and is commonly overgrown by reddish-brown
446 (sl_{1rb}), yellowish-brown (sl_{1yb}), and yellow (sl_{1y}) sphalerite ([Figs. 3B-C, 4B-C](#)). Under the
447 petrographic microscope, black sphalerite (sl_{1bl}) forms micro- to millimeter-sized anhedral to
448 subhedral crystals often intergrown with fine-grained DRD ([Figs. 4A-C](#)).

449 Sphalerite that crystallized during the second mineralization step is recognized by generally
450 lighter colors and replacement and crosscutting (mostly in steep veins) relationships with
451 sphalerite and other minerals (e.g., notably, WSD_1 ; [Figs. 3F-I](#)) of the first mineralization step.
452 Sphalerite formed during the second mineralization step (sl_2) is volumetrically restricted. It
453 occurs as micro- to millimeter-sized anhedral to subhedral crystals in microfractures and open

454 spaces, mostly intergrown with WSD₂ (Figs. 4D, G-H) and, in places, partially replacing
455 sphalerite of the first mineralization step and DRD (Figs. 3G-H, 4E-F). The sequence of the
456 second mineralization step starts with orange sphalerite (sl_{2o}), which is frequently epitaxially
457 overgrown by yellow (sl_{2y}) and white (sl_{2w}) sphalerite (Figs. 4D, H). White sphalerite also occurs
458 as veinlets that crosscut black sphalerite (sl_{1bl}), WSD₁, and WSD₂ (Figs. 3I; 4A, F).

459 Different textural types of pyrite have been distinguished in the studied samples, all with sizes
460 of <400 µm: i) fine disseminations in sl₁ (Figs. 4A-C, I), ii) pseudomorphic pyrite according to
461 disseminated marcasite in DRD (Fig. 4G), and iii) subhedral-euhedral crystals in fractures and
462 cavities of sl₁ (Fig. 4A). In the studied samples, galena occurs as i) subhedral crystals in WSD₁
463 and WSD₂ (Fig. 3B), often filling spaces (Fig. 4I), and ii) in fine veinlets that cut WSD₁ and
464 WSD₂ (Fig. 3D). Locally, galena is intergrown with anhedral aggregates of gratonite.

465 From the above-described textural relationships, a general paragenetic sequence has been
466 produced for the studied samples (Fig. 5), the deposition sequence being also broadly
467 consistent with petrographic descriptions by Fontboté and Gorzawski (1990) and Spangenberg
468 et al. (1999). New is the recognition of the volumetrically minor mineralization formed during a
469 second step with its conspicuous orange (sl_{2o}) and yellow (sl_{2y}) sphalerite.

470 In the Chilpes prospect, sulfide mineralization mostly occurs as sphalerite and galena with
471 minor proportions of pyrite in coarse-grained white sparry dolomite (Figs. S1A-B, S2, Electronic
472 Supplementary Material). In addition, two bands a few centimeters in thickness of massive,
473 coarse-grained pyrite (up to 0.5 cm) are observed (Fig. S1C). Sphalerite color grades from
474 reddish-brown (sl_{1rb}) to yellowish-brown (sl_{1yb}), orange (sl_o), and yellow (sl_y; Figs. S2A-F). In
475 general, sphalerite has a "dirty" appearance (e.g., Fig. S2A, C, E), due to the presence of
476 abundant tiny inclusions of dolomite and subordinately, pyrite, indicating that sphalerite is to a

477 large extent of replacive nature similarly to a part of WSD that reveals ghosts of grainstone
478 oolites (Fig. S2L). Sphalerite of reddish-brown (sl_{rb}) and yellowish-brown (sl_{yb}) colors appears
479 mainly intergrown with coarse-grained WSD and also within massive pyrite and usually forms
480 aggregates of grains that are up to 1 cm in size individually (Fig. S2A-F). Reddish-brown (sl_{rb})
481 sphalerite may grade towards yellowish-brown (sl_{yb}) color toward the border of individual grains
482 (Fig. S2B). Orange (sl_o) and yellow (sl_y) sphalerite has been only found intergrown with coarse-
483 grained WSD (Fig. S2G-L). Galena appears mostly as grains <1 cm in size, mainly as open-
484 space filling within the coarse-grained WSD; it is also observed as thin veinlets that crosscut
485 WSD and in the massive pyrite bands (Fig. S2G-J).

486 In the studied sample from the Huacrash prospect, sphalerite forms anhedral grains that are
487 up to 1 cm in size and display brownish-orange (sl_{bo}) color cemented by WSD (Fig. S3A-F). As
488 in Chilpes, sphalerite grains show abundant micro-inclusions and irregular, corroded
489 boundaries and are veined by dolomite. Galena is scarce and appears as anhedral grains less
490 than 100 µm in size (Fig. S3A-B).

491 Study by reflected light microscope coupled with a cold-stage cathodoluminescence (CL)
492 system reveals oscillatory and sector zoning in orange and yellow sphalerite from Chilpes
493 (sample FSV50) in contrast with weak or nil CL response in sphalerite formed during the first
494 mineralization step (Fig. S4).

495 *Shalipayco deposit*

496 Sphalerite constitutes the main ore mineral, and appears along with traces of galena, pyrite,
497 and marcasite. The main gangue mineral is dolomite; other gangue minerals in minor amounts
498 include barite, calcite, and quartz. Two generations of dolomite were recognized in the studied

499 samples: i) dolomite 1 (dol₁), which occurs as replacement of the host limestone and contains
500 interstitial early sphalerite, and ii) dolomite 2 (dol₂) which is coarser-grained and intergrown with
501 late sphalerite. These textural features are consistent with those described by [de Oliveira et al.](#)
502 [\(2021\)](#).

503 The sphalerite grains are between ~20 µm and 1 mm in size and are largely free of visible
504 inclusions of other sulfides. According to [de Oliveira et al. \(2021\)](#), there was a single ore-forming
505 episode at Shalipayco. Following the same criteria as for the discrimination of sphalerite types
506 in San Vicente, five types of sphalerite were recognized: black (sl_{bl}), reddish-brown (sl_{rb}),
507 yellowish-brown (sl_{yb}), yellow (sl_y), and white (sl_w; *var. cleiophane*). Black sphalerite (sl_{bl})
508 appears as micro- to millimeter-sized anhedral to subhedral crystals with rectilinear and sub-
509 roundish grain boundaries ([Figs. 6A-D](#)). Black sphalerite (sl_{bl}) is commonly intergrown with
510 pyrite aggregates and tiny (< 20 µm) prismatic crystals of marcasite ([Figs. 6A, C](#)). Reddish-
511 brown sphalerite (sl_{rb}) forms anhedral to subhedral grains chiefly grown on black sphalerite (sl_{bl})
512 and overgrown by yellowish-brown sphalerite (sl_{yb}; [Figs. 6E-H](#)). In places, reddish-brown (sl_{rb})
513 and yellowish-brown (sl_{yb}) sphalerite appears interstitially between barite crystals ([Figs. 6E-F](#))
514 and as open space filling together with dol₂ ([Figs. 6G-J](#)). Yellow sphalerite (sl_y) appears as
515 anhedral grains that grew on yellowish-brown sphalerite (sl_{yb}; [Figs. 6G-L](#)) whereas white
516 sphalerite (sl_w) forms small anhedral grains in contact with yellow sphalerite (sl_y; [Figs. 6K-L](#)).

517 Two different textural types of pyrite have been observed: i) subhedral to anhedral grains <200
518 µm in size as void and fracture-filling in dol₁, commonly intergrown with black sphalerite (sl_{bl};
519 [Figs. 6A-B](#)) and ii) fine to medium-grained subhedral to euhedral cubic crystals <10 µm, as
520 dissemination and within microfractures in dol₁ and dol₂, and at borders of yellowish-brown (sl_{yb})

521 and yellow (sl_y) sphalerite types (Figs. 6E-J). Traces of galena occur in voids and narrow
522 veinlets that crosscut yellowish-brown (sl_{yb}) and yellow sphalerite (sl_y; Figs. 6I-J).

523 Taking into account the aforementioned petrographic observations as well as textural
524 descriptions carried out by de Oliveira et al. (2021), a paragenetic sequence has been produced
525 for the Shalipayco deposit (Fig. 7).

526 **Sphalerite geochemistry**

527 A summary of sphalerite compositions (LA-ICP-MS and EMPA data), including minimum,
528 maximum, median, mean, and interquartile range (IQR) values is presented in Table 1. LA-ICP-
529 MS results are presented in box-and-whisker plots (Fig. 8). At Shalipayco, only trace element
530 analyses for reddish-brown (sl_{rb}), yellowish-brown (sl_{yb}), and yellow (sl_y) sphalerite types were
531 obtained. In addition, EMPA and LA-ICP-MS analyses of sphalerite from the MVT Cristal
532 deposit obtained by Mondillo et al. (2018b) are shown for comparison. A significant effort was
533 made to report only the content of elements whose variations respond to solid solutions and
534 not to mixed mineral analyses (e.g., presence of mineral micro-inclusions) by selecting only flat,
535 stable signal intervals from the LA-ICP-MS spectra. Of the analyzed elements, Sb, As, Tl, and
536 Pb gave occasionally spiky LA-ICP-MS transient signals, possibly indicative of micro-scale solid
537 inclusions (e.g., galena).

538 Sphalerite from the San Vicente and Shalipayco deposits displays a relatively wide range of
539 minor and trace element contents. Amongst these, Fe and Cd are the only elements that
540 reached contents higher than 1 wt%. In sphalerite from the San Vicente deposit, Fe contents
541 measured with LA-ICP-MS (IQR = 2.0-0.55 wt%, up to 4.3 wt%) are broadly comparable with
542 those measured with EMPA (IQR = 2.4-0.64 wt%, up to 4.7 wt%; Table 1). In this deposit, Fe

543 contents show a pronounced depletion in sphalerite from the first (sl₁; mostly > 1 wt%) to the
544 second (sl₂; systematically < 125 ppm) mineralization steps. Within the first step, a gradual
545 decrease from sl_{1bl} to sl_{1y} is recognized (Fig. 8A). In sphalerite grains from the Chilpes prospect,
546 Fe contents are generally low (< 187 ppm), much lower in reddish-brown (sl_{rb}; IQR = 9.4-9.0
547 ppm) and yellowish-brown (sl_{yb}; IQR = 9.5-9.0 ppm) than in orange (sl_o; IQR = 102-87 ppm)
548 and yellow (sl_y; IQR = 128-93 ppm) sphalerite. Sphalerite grains from the Huacrash prospect,
549 of brownish-orange color (sl_{bo}), yielded highly variable Fe contents with an IQR of 0.26 wt%-
550 8.0 ppm. In Shalipayco, the Fe content (IQR = 0.20-0.07 wt%, up to 3.7 wt%) decreases from
551 reddish-brown (sl_{rb}) to yellow (sl_y) sphalerite types. Iron values in sphalerite from the Cristal
552 deposit (EMPA data: IQR = 9.95-6.2 wt%) are higher compared to sphalerite from San Vicente
553 and Shalipayco. Zinc shows a negative correlation with Fe (Fig. S5 in Electronic Supplementary
554 Material), pointing to the commonly observed dominant Fe²⁺ ↔ Zn²⁺ simple substitution (Johan
555 1988; Cook et al. 2009) when Fe > ~1 wt%.

556 Cadmium contents are broadly comparable in sphalerite of the second mineralization step (sl₂)
557 of the San Vicente deposit (IQR = 0.57-0.34 wt%), in sphalerite from the Chilpes (IQR = 1.0-
558 0.50 wt%) and Huacrash (IQR = 0.79-0.74 wt%) prospects, and in sphalerite from the
559 Shalipayco deposit (IQR = 0.45- 0.27 wt%). These values are comparable to those reported by
560 Mondillo et al. (2018b) in sphalerite from Cristal (IQR = 0.59-0.26 wt%), and higher than those
561 of sphalerite from the first mineralization step (sl₁) at San Vicente (IQR = 0.11-0.05 wt%; Fig.
562 8B).

563 As for the critical elements (i.e., Ge, Ga, and In), sphalerite from the San Vicente deposit shows
564 significantly higher Ge contents in grains from the second mineralization step (sl₂; IQR = 566-
565 41 ppm), particularly in orange (sl_{2o}; IQR = 1,207-375 ppm, up to 1,861 ppm) and yellow (sl_{2y};

566 IQR = 269-130 ppm, up to 1,096 ppm) sphalerite types relative to sphalerite from the first
567 mineralization step (sl₁; IQR = 91-44 ppm); white sphalerite (sl_{2w}) yielded, however, the lowest
568 Ge values (IQR = 0.23-0.14 ppm, up to 2.1 ppm) among all analyzed sphalerite types (Fig. 8C).
569 Sphalerite from Chilpes yielded variable Ge contents, which were higher in reddish-brown (sl_{rb};
570 IQR = 445-22 ppm, up to 1,745 ppm), orange (sl_o; IQR = 172-96 ppm), and yellow (sl_y; IQR =
571 164-55 ppm) than in yellowish-brown (sl_{yb}; IQR = 11-5 ppm) types. Sphalerite from Huacrash
572 yielded Ge contents with an IQR of 650-34 ppm (up to 855 ppm). In Shalipayco, the highest Ge
573 values were registered in yellow sphalerite (sl_y; IQR = 375-267 ppm, up to 1,119 ppm). Despite
574 the fact that the highest individual Ge values were found in sphalerite from the second step of
575 mineralization at San Vicente, sphalerite from Shalipayco yielded, on average, higher Ge
576 contents (Table 1; Fig. 8C). Sphalerite from the Cristal deposit also has significant Ge contents
577 (IQR = 231-31 ppm, up to 386 ppm).

578 The highest Ga values were obtained for the reddish-brown sphalerite (sl_{rb}; IQR = 1,156-0.26
579 ppm, up to 3,943 ppm) from the Chilpes prospect, whereas the yellowish-brown (sl_{yb}; IQR = 10-
580 0.9 ppm), orange (sl_o; IQR = 0.7-0.2 ppm), and yellow (sl_y; IQR = 1.4-0.1 ppm) sphalerite types
581 at this site yielded lower Ga contents. In the San Vicente deposit, Ga reaches maximum values
582 in sphalerite from the second mineralization step (sl₂; IQR = 93-15 ppm), particularly in orange
583 sphalerite (sl_{2o}; IQR = 200-12 ppm, up to 997 ppm; Fig. 8D). Sphalerite from Huacrash yielded
584 an IQR for Ge of 97-50 ppm. In sphalerite from Shalipayco and Cristal, Ga values were
585 systematically <7 ppm and down to ~ 0.1 ppm.

586 Indium contents in sphalerite from San Vicente, Shalipayco, and Cristal deposits are
587 systematically low, mostly at the sub-ppm level (Fig. 8E). The highest In values were recorded
588 in reddish-brown sphalerite from Chilpes (sl_{rb}; IQR = 26-0.021 ppm, up to 92 ppm), and in

589 orange sphalerite from the San Vicente deposit (sl_{2o} ; IQR = 8.2-2.2 ppm, up to 18 ppm). Other
590 elements that occur in trace amounts – commonly between a few ppm to some hundreds of
591 ppm – are Mn (Fig. 8F), Cu (Fig. 8G), Ag (Fig. 8H), As (Fig. 8I), and Hg (Fig. 8J).

592 **Nanostructure of sphalerite**

593 The thin foil #1, prepared from sample 2019-SV-05, covers a portion of black sphalerite (sl_{1bl})
594 and a larger area of white sphalerite (sl_{2w}) in discontinuous contact (Fig. 9A). The HAADF-
595 STEM images reveal general crystal homogeneity within the black sphalerite and the presence
596 of a set of identically oriented nano-sized (≤ 250 nm) crystalline fringes within white sphalerite
597 (Figs. 9A, 10A, C). These images combined with the TEM-EDS area mapping also reveal
598 chemical homogeneity in both the white and black sphalerite, regardless the occurrence of
599 fringes, except for the presence of a pyrrhotite inclusion (Fig. 9A). The measured d-spacing
600 from the SAED collected from the black sphalerite cluster at ~ 1.95 Å, very close to the ideal
601 1.9405 Å of plane (110) in the hexagonal $2H$ structure polytype in wurtzite (Fig. 10B). In
602 contrast, the white sphalerite sampled in this thin foil exhibits larger d-spacings from 2.850 to
603 3.047 Å; the former has not been reported previously for sphalerite, whereas the latter is very
604 close to the ideal 3.0483 Å of plane (104) in the hexagonal $10H$ wurtzite polytype (Fig. 10D).
605 Noteworthy, HRTEM images show no significant mismatch of plane orientation between fringes
606 corresponding to stacking fault defects and matrix in white sphalerite but a remarkable
607 polycrystalline nature.

608 The inner portion of the yellow (sl_{2y}) sphalerite sampled by the thin foil #2 (prepared from sample
609 2019-SV-15A) also exhibits nano-sized crystalline fringes and chemical homogeneity (Fig. 9B).
610 The HRTEM imaging and the SAED show a wide range of d-spacings from 2.706 to 3.150 Å,

611 also within a polycrystalline matrix, matching hkl common to the cubic 3C of and hexagonal
612 10H structures of sphalerite and wurtzite, respectively (Figs. 10E-H).

613 The HAADF-STEM imaging along with TEM-EDS mapping (Fig. 9C) of the thin foil #3 (from
614 sample 2019-SV-15B) reveals crystal and compositional homogeneity within the orange
615 sphalerite (sl_{2o}), despite the polycrystalline nature of the matrix (Fig. 10I). The measured d-
616 spacing from the SAED of 3.01 Å (Fig. 10J) accords well with the (104) of the 10H structure of
617 wurtzite. D-spacings measured from the HRTEM images are in the range between 2.513 and
618 3.308 Å (Figs. 10K-L), therefore being also very close to the ideal 2.5244 Å, 2.7933 Å, and
619 3.3117 Å of the planes (108), (106), and (111), respectively.

620 The cross-section of the thin foil #4 (from sample 2019-SV-15B) reveals discontinuity along the
621 contact between white (sl_{2w}) and yellow (sl_{2y}) sphalerite as well as chemical homogeneity within
622 each sphalerite type (Fig. 9D). These two types of sphalerite consist of a polycrystalline matrix
623 made up of an aggregation of crystalline domains with a range of orientations. The d-spacing
624 measured from SAED and HRTEM images for the white sphalerite range from 1.65 Å to 5.403
625 Å, which matches the ideal plane (311) and theoretical cell parameter of cubic 3C sphalerite,
626 respectively, as well as the d-spacing 2.789 Å, 2.515 Å, and 3.12 Å documented for the 10H
627 structure of wurtzite (Figs. 10M-N). The latter is also identified (1.65 Å to 3.03 Å) for yellow
628 sphalerite (Figs. 10O-P).

629 Discussion

630 *Enrichment of MVT sphalerite in Ge and Ga*

631 In San Vicente, sphalerite deposited during the first mineralization step, which is the
632 volumetrically most abundant in this deposit, yielded Ge contents (IQR = 91-44 ppm; Table 1)

633 similar to sphalerite from other MVT deposits in Peru (Cristal: IQR = 231-31 ppm, up to 386
634 ppm Ge; [Mondillo et al. 2018b](#)) and worldwide (normal range between 10 and 300 ppm, [Paradis](#)
635 [2015](#); about 400 ppm in MVT zinc ore concentrate, [Shanks et al. 2017](#)). The Ge content is
636 remarkably higher in sphalerite of the volumetrically minor second mineralization step at the
637 San Vicente deposit, particularly in orange sphalerite (sl_{2o} , IQR = 1,207-375 ppm, up to 1,861
638 ppm; [Fig. 8C](#)); to a lesser extent, also in sphalerite from the Chilpes (IQR = 193-20 ppm, up to
639 1,741 ppm) and Huacrash (IQR = 650-34 ppm, up to 855 ppm) prospects in the San Vicente
640 district. In Shalipayco, yellow sphalerite (sl_y) is the one showing the highest Ge contents (IQR
641 = 375-267 ppm, up to 1,119 ppm) in this deposit. The aforementioned maximum Ge values for
642 sphalerite in Peruvian MVT deposits are comparable with those obtained in Ge-rich sphalerite
643 from the Tres Marías deposit in Mexico (average = 960 ppm, up to 3200 ppm; [Saini-Eidukat et](#)
644 [al. 2009](#)), which for some authors is a MVT deposit and for others is of magmatic affiliation (see
645 discussion in [Ostendorf et al. 2017](#)), as well as with sphalerite deposited during the low-
646 temperature stage (140-80 °C) of the Saint Salvy vein-type deposit (up to 2,600 ppm of Ge;
647 [Belissont et al. 2014](#)). Noteworthy, in the porphyry-related Cordilleran polymetallic deposits of
648 the Morococha District (central Peru), only local, late, low-temperature, colloform sphalerite
649 shows relatively high Ge values (IQR = 129-74 ppm, up to 215 ppm; [Benites et al. 2021](#)). At
650 generally lower contents, Ga also shows contrasting values amongst the analyzed sphalerite
651 types and localities ([Fig. 8D](#); [Table 1](#)). Similar to Ge, Ga contents are also higher in sphalerite
652 from the second mineralization step at the San Vicente deposit and in sphalerite from Chilpes
653 (with some peaks of up to 3,943 ppm) and Huacrash relative to sphalerite of the first
654 mineralization step at the San Vicente deposit. Sphalerite from the Shalipayco and Cristal
655 deposits shows low Ga contents ([Table 1](#)). Finally, In content in sphalerite from the San Vicente

656 district and the Shalipayco deposit, as expected in MVT deposits (Cook et al. 2009; Ye et al.
657 2011, 2016; Yuan et al. 2018), is systematically low (mostly < 1 ppm).

658 Even if systematic trends in the Ge and Ga contents have been determined, there is a relatively
659 large variation range within each sphalerite type/locality (Fig. 8C-D) and even within single
660 crystals. This fact could be related to oscillatory and sector element zoning as mapped in Ge-
661 rich sphalerite through CL imaging (e.g., in orange and yellow sphalerite from Chilpes; Fig. S4
662 in Electronic Supplementary Material). CL activator or and/or co-activator elements in the
663 sphalerite structure include Cd, Mn, and Hg (Çiftçi 2009), which have higher values in sphalerite
664 grains from the second mineralization step in the San Vicente deposit and from Chilpes and
665 Huacrash (i.e., those that are also richer in Ge; Fig. 8).

666 The minor and trace element contents in sphalerite from the studied Peruvian MVT return
667 variable crystallization temperatures calculated with the GGIMFis geothermometer of Frenzel
668 et al. (2016) (Table 2). Despite the large error associated with the method, the obtained
669 temperatures fall mostly within the 50 – 200°C bracket typical of mineralizing fluids in MVT
670 systems (Leach et al. 2005). Sphalerite from Cristal, which is unusually Fe-rich for a MVT
671 deposit (Mondillo et al. 2018b), yielded higher crystallization temperatures ($234 \pm 77^\circ\text{C}$, 2-sigma
672 error; Fig.12). In the San Vicente deposit, there is a sharp decrease of the calculated sphalerite
673 crystallization temperature from the first mineralization step, at around 180°C, to the second
674 mineralization step, at around 50°C. Sphalerite from the Chilpes and Huacrash prospects would
675 have crystallized at similar temperatures as sphalerite from the second mineralization step in
676 the San Vicente deposit. In the Shalipayco deposit, sphalerite records a progressive decrease
677 in the crystallization temperature from around 130°C to 60°C from reddish-brown to yellow
678 sphalerite.

679 For the San Vicente district, the two mineralization steps correlate with the aforementioned
680 sphalerite compositional groups, defined in terms of Ge and Ga contents and crystallization
681 temperatures, and those determined by Bastian (2021) based on Pb isotope ratios. Thus,
682 sphalerite from the second mineralization step at the San Vicente deposit and from the Chilpes
683 and Huacrash prospects (i.e., Ge- and Ga-rich) is characterized by less radiogenic Pb isotope
684 signatures than sphalerite from the first mineralization step at the San Vicente deposit (i.e., Ge-
685 and Ga-depleted; Fig. 8C-D). The less radiogenic signature of the former can be due to
686 dominant metal sourcing from Mitu Group rocks as already suggested for similar low-radiogenic
687 Pb isotope signatures of Shalipayco galena (Fontboté et al. 1990). More radiogenic signatures
688 could be related to additional metal sourcing from older basement rocks (Fontboté and
689 Gorzawski 1990; Chiaradia and Fontboté 2003) and/or hydrocarbon-related fluids (Bastian
690 2021). Although Luo et al. (2022) have recently linked higher Ge contents in sphalerite from
691 carbonate-hosted Zn deposits in China with mineralizing fluids scavenging Ge from Ge-rich
692 basement rocks, the available Pb isotope data of the MVT belt in the Pucará Group do not
693 permit to assign Ge and Ga sphalerite enrichment to specific source rocks.

694 *Incorporation mechanisms of Ge and Ga into sphalerite*

695 The mineralogical expression of Ge, Ga and other elements found in minor and trace amounts
696 is assessed from a nano-mineralogical and compositional point of view in the following. TEM-
697 EDS mapping on samples from San Vicente shows chemical homogeneity within all analyzed
698 sphalerite types and lack of mineral inclusions, except for the anecdotic presence of pyrrhotite
699 nano-inclusions in black sphalerite (Fig. 9A). Therefore, high contents of such trace elements
700 detected by LA-ICP-MS in the analyzed sphalerite cannot be attributed to the presence of nano-
701 to-micron sized inclusions. It is worth to note that black sphalerite from San Vicente (sl_{1b}) yielded

702 d-spacings of $\sim 1.95 \text{ \AA}$, which are significantly lower than those of neighboring white sphalerite
703 (sl_{2w} ; 3.0483 \AA) despite both sphalerite types exhibiting an identical wurtzite-type $2H$ structure.
704 In contrast, the wider range of variation of d-spacing observed in yellow sphalerite (sl_{2y} ; 1.65 to
705 3.15 \AA) is related to the coexistence of conversion of the cubic $3C$ to hexagonal wurtzite-type
706 $10H$ structure, which was apparently complete in the orange sphalerite (sl_{2o}) from this locality,
707 displaying higher d-spacings between 2.513 and 3.308 \AA , which have been exclusively reported
708 in the wurtzite-type $10H$ structure. Coexistence of cubic and hexagonal polytype structures
709 between (non)-paragenetic sphalerite grains and within single sphalerite grains have already
710 been noted by other authors in several hydrothermal deposits and demonstrated to be
711 promoted by screw dislocations and twin mechanisms (Pósfai et al. 1988; Bente et al. 1998;
712 Šrot et al. 2003; Ciobanu et al. 2011; Cook et al. 2015b; Xu et al. 2022). There is an infinite
713 number of different stacking sequences (polytypes) that are possible between the ideal cubic
714 and hexagonal structures (Ciobanu et al. 2011). Various polytypes and polytypic sequences,
715 both ordered and disordered, have been documented from both synthetic and natural sphalerite
716 and conversion between structures has been debated in terms of incorporation of exotic
717 elements accommodated by structural modification (e.g., Scott and Barnes 1972; Sokol et al.
718 2020; Xu et al. 2022).

719 In the sphalerite grains from the four studied deposits and prospects, binary positive elemental
720 correlations seem to be consistent with lattice bound incorporation of elements indeed related
721 with substitution mechanism not readily detectable under HRTEM observations. Thus, positive
722 correlations between Ge and Cu as those observed for some second-step yellow (sl_{2y}) and
723 orange (sl_{2o}) sphalerite types in the San Vicente deposit and in sphalerite from the Chilpes
724 prospect (Fig. 11A) lead us to suggest a $2Cu^+ + Ge^{4+} \leftrightarrow 3Zn^{2+}$ coupled substitution, also
725 documented in other deposits (Belissont 2016; Belissont et al. 2016; Bonnet et al. 2016; Wei et

726 al. 2019; Cave et al. 2020; Liu et al. 2022). A positive correlation is also recognized between
727 Ge and Ag, partially lying along the ~1:2 ratio line (Fig. 11B). This correlation is mainly noticed
728 for second-step orange (sl_{2o}) sphalerite from San Vicente, most sphalerite types from Chilpes
729 and Huacrash, and yellowish-brown (sl_{yb}) and yellow (sl_y) sphalerite from Shalipayco,
730 suggesting a $\text{Ge}^{4+} + 2\text{Ag}^+ \leftrightarrow 3\text{Zn}^{2+}$ coupled substitution as previously proposed by Cook et al.
731 (2009) and Belissont et al. (2014). A fairly positive correlation between the molar contents of
732 Ge and Tl in San Vicente and Shalipayco (Fig. 11C) is observed. The aforementioned
733 correlations indicate that incorporation of Ge in the studied sphalerite was coupled with the
734 incorporation of monovalent Cu, Ag, and Tl (Fig. 11D), and that combinations of these coupled
735 substitution schemes (i.e., $\text{Ge}^{4+} + 2(\text{Cu} + \text{Ag} + \text{Tl})^+ \leftrightarrow 3\text{Zn}^{2+}$) are plausible.

736 As for Ga and In contents, they show no correlation with Ge (Figs. 11E-F), suggesting
737 incorporation via other independent substitution mechanisms. Rough correlations between Ga
738 and In (Fig. 11G) and of Ga and Sn (Fig. 11H) suggest coupled substitutions of these elements
739 in sphalerite. Occasional positive correlation between Cu and Ga + In + Sn at ~1:1 (Fig. 11I),
740 especially in second-step white (sl_{2w}) and some yellow (sl_{2y}) sphalerite from the San Vicente
741 deposit and sphalerite from Chilpes, seems to suggest $\text{Cu}^+ + (\text{Ga}, \text{In})^{3+} + \text{Sn}^{4+} \leftrightarrow 4\text{Zn}^{2+}$ coupled
742 substitutions. However, there is a set of data, which includes the rest of the analyzed sphalerite
743 grains from San Vicente, Chilpes, Shalipayco, and Cristal that lies far above the Cu: Ga + In +
744 Sn = 1:1 correlation line (Fig 11I), pointing to higher Cu at a given Ga + In + Sn content, probably
745 due to the fact that Cu is also involved in coupled substitutions for the incorporation of Ge,
746 which is normally more abundant than Ga and In in the analyzed sphalerite.

747 *Color of sphalerite vs. chemical composition*

748 The most common names used to refer to sphalerite varieties according to crystal color include
749 i) cleiophane (Palache et al. 1944), characterized by high transparency and by white color or
750 being colorless, ii) ruby blende (Dana 1892), with red shades, and iii) marmatite (Boussingault
751 1830; Palache et al. 1944), highlighted by its black color and opacity. Other less commonly
752 used variety names for sphalerite include iv) golden sphalerite, with yellow to orange shades,
753 and v) green sphalerite, among others. The use of these varietal names does not follow any
754 criteria of specific element content ranges, crystal-chemical or structural parameters. The only
755 proposal to define a particular sphalerite variety based on its chemical composition was made
756 by Ramdohr (1980), who suggested that Fe should be equal to, or greater than, 10 wt% in
757 marmatite. In the following we explore possible correlations between color and composition.

758 Iron is considered the most ubiquitous impurity element in sphalerite (Di Benedetto et al. 2005)
759 and for many years there has been a consensus that sphalerite color is directly and essentially
760 dependent on Fe content (Awadh 2009; Cook et al. 2009; Li and Barnes 2019; Knorsch et al.
761 2020). However, this principle is not always fulfilled, particularly in Fe-poor sphalerite (< 2-3
762 wt% Fe; see Roedder and Dwornik 1968), as it is the case of most analyzed sphalerite samples
763 (Table 1). In sphalerite from the San Vicente deposit, there is a general decrease in the Fe
764 content from earlier (darker) to later (lighter) types; such Fe depletion is, however, not
765 continuous and shows an abrupt depletion from first-step (including black [sl_{1bl}], reddish-brown
766 [sl_{1rb}], yellowish-brown [sl_{1yb}], and yellow [sl_{1y}] types) to second-step (including orange [sl_{2o}],
767 yellow [sl_{2y}], and white [sl_{2w}] types; Fig. 8A) sphalerite.

768 Black sphalerite is often related to higher Fe content (Craig and Vaughan 1994; Katsev et al.
769 2001). However, Fe contents do not necessarily have to be high to produce such color, as
770 observed in black sphalerite from San Vicente (sl_{1bl}, IQR = 2.6-1.7 wt% Fe) and other MVT

771 deposits elsewhere ([Bradbury 1961](#); [Jolly and Heyl 1964](#); [Roedder and Dwornik 1968](#)), with
772 contents even lower than those recorded in this study. In general, black sphalerite in San
773 Vicente replaces the host rock, is fine-grained and contains impurities of other minerals
774 (dolomite, pyrite) and, as identified in the present work by FIB-TEM, nano-inclusions of
775 pyrrhotite, which could explain its dark color.

776 Reddish-brown sphalerite in the San Vicente (sl_{1rb}) and Shalipayco (sl_{rb}) deposits also has low
777 Fe contents (IQR = 2.1-1.1 wt%), and extremely low Fe contents are found in reddish-brown
778 sphalerite from Chilpes (sl_{rb}; mostly <d.l.). Reddish-brown sphalerite from the three localities
779 may show significant enrichment in Cd (particularly in Chilpes and Shalipayco; [Fig. 8B](#)), Cu
780 (Chilpes and Shalipayco; [Fig. 8G](#)), Mn (Chilpes; [Fig. 8F](#)), Hg (Shalipayco; [Fig. 8J](#)), Ge (Chilpes
781 and Shalipayco; [Fig. 8C](#)), and Ag (Shalipayco; [Fig. 8H](#)), thus suggesting that some of these
782 elements could have an impact on crystal color. [Sapalski and Gómez \(1992\)](#) determined that
783 red sphalerite from the Áliva MVT mine in Santander, Spain, coincides with high Ge and Hg
784 contents, whereas [Sanabria and García-Álvarez \(2005\)](#) correlated this color with high Cd, Cu,
785 and Hg contents.

786 Yellowish-brown sphalerite has been identified in San Vicente (sl_{1yb}), Chilpes (sl_{yb}), and
787 Shalipayco (sl_{yb}). Again, Fe content alone – with variations of more than three orders of
788 magnitude between yellowish-brown sphalerite from the three localities ([Fig. 8A](#)) – cannot
789 explain this color. Yellowish-brown may be considered an intermediate color tone between
790 reddish-brown and yellow. [Kelley et al. \(2004\)](#) suggested correlation of yellow sphalerite with
791 relatively high As and Hg contents. The highest As values in our study were not found in
792 sphalerite of yellow color but in sphalerite of reddish-brown color at Chilpes (sl_{rb}, IQR = 480-60
793 ppm, up to 1,857 ppm; [Fig. 8I](#)). Yellow sphalerite from the first mineralization step at San Vicente

794 (sl_{1y}) yielded the highest As content (IQR = 145-7.5 ppm) among analyzed yellow sphalerite,
795 whereas yellow sphalerite from Shalipayco (sl_y; IQR = 5.1-3.4 ppm), Chilpes (< 11 ppm), and
796 the second mineralization step at San Vicente (sl_{2y}; IQR = 5.1-3.4 ppm) yielded much lower As.
797 Therefore, we do not observe a systematic correlation between the yellow color and high As
798 contents in the studied samples. On the other hand, Hg contents are not high in the analyzed
799 yellow sphalerite from the three localities compared to the other sphalerite types (Fig. 8J).
800 Yellow cyclic growth bands of sphalerite have been correlated with higher Ge, Cu, and Pb
801 contents in the North German Basin (Knorsch et al. 2020). Germanium is relatively high in
802 yellow sphalerite in the studied samples compared to other sphalerite types from the respective
803 localities and could therefore explain, in part, this color. Slack et al. (1966, 1967) suggested
804 that the absorption band of Fe²⁺ and Zn²⁺ (blue), added with the absorption of small amounts
805 of Co²⁺ (red), compound the yellow color. This does not seem to be the case for the studied
806 sphalerite samples as all of them yielded very low Co contents, mostly below the detection limit.

807 Orange sphalerite from San Vicente (sl_{2o}) displays relatively high contents of Cu, Ge, Ag, and
808 Cd (Fig. 8). Orange sphalerite from Chilpes (sl_o) and brownish-orange sphalerite from Huacrash
809 (sl_{bo}) are also relatively enriched in Ge and Cd, and to some extent also in Ag, but not in Cu.
810 High Cd is also reported in orange sphalerite from Áliva (Gómez-Fernández et al. 2000).

811 Finally, white sphalerite is mainly correlated with very low Fe contents (Ramdohr 1980). Iron in
812 white sphalerite from the San Vicente deposit (sl_{2w}) is indeed not detectable. White sphalerite
813 (sl_{2w}) is also depleted in most of the other analyzed minor and trace elements with the
814 remarkable exceptions of Cd, Ga, Mn, and Hg, which are relatively high compared to other
815 sphalerite types from the same locality (Fig. 8). Therefore, we conclude that the role of some
816 long-considered chromophore elements in sphalerite (i.e., Cd, Mn, Hg) *per se* should be

817 reconsidered. Occasional pale green internal reflections in white sphalerite could be linked to
818 trace contents of Co (Hofmann and Henn 1985; Rager et al. 1996).

819 The above observations suggest possible relationship between sphalerite color and abundance
820 of certain trace elements. Regarding Ge, high contents of this metalloid seem to be correlated
821 with orange, and to lesser extent, yellow, colors in sphalerite. However, it is challenging to affirm
822 which element or combination of elements and under which oxidation states could directly
823 influence crystal colors since not enough evidence has been found yet. Unfortunately, we are
824 not far from the conclusions reached by Roedder and Dwornik (1968), who stated that “the true
825 coloring mechanism is not known” in sphalerite.

826 **Conclusions**

827 LA-ICP-MS analyses on sphalerite have been performed after a thorough petrographic study
828 of ore samples from the MVT San Vicente district (including the San Vicente deposit and the
829 Chilpes and Huacrash prospects) and the Shalipayco deposit in Peru. The results make it
830 possible to correlate trace element contents with sphalerite types and fluid evolution.

831 In the analyzed samples, all types of sphalerite show substantial Ge contents (IQR = 118-44
832 ppm), as is typical in MVT mineralization. The highest Ge values (> 1,000 ppm) from the studied
833 deposits were found in Fe-poor sphalerite that crystallized relatively late in the paragenetic
834 sequences and probably from fluids of lower temperature relative to Ge-poorer sphalerite.
835 Gallium contents are, in general, lower than those of Ge. However, very high Ga values (>
836 3,000 ppm) are found in Fe-poor sphalerite from Chilpes. A correlation between Ga enrichment
837 and mineralization sequence could not be determined. According to the obtained values, certain

838 sphalerite types from the studied Peruvian MVT deposits are among the most enriched in Ge
839 and Ga globally.

840 HRTEM observations revealed that trace elements detected in high amounts in the analyzed
841 sphalerite types are lattice-bound. Correlations between molar contents suggest incorporation
842 of Ge into the sphalerite crystal lattice coupled with monovalent cations through substitution
843 schemes such as $\text{Ge}^{4+} + 2\text{Cu}^+ \leftrightarrow 3\text{Zn}^{2+}$, $\text{Ge}^{4+} + 2\text{Ag}^+ \leftrightarrow 3\text{Zn}^{2+}$, and $\text{Ge}^{4+} + 2(\text{Cu} + \text{Ag} + \text{Tl})^+ \leftrightarrow 3\text{Zn}^{2+}$. Gallium contents do not correlate with Ge contents, thus suggesting incorporation via
844 other independent substitution mechanisms such as $\text{Cu}^+ + (\text{Ga}, \text{In})^{3+} + \text{Sn}^{4+} \leftrightarrow 4\text{Zn}^{2+}$ coupled
845 substitutions.
846

847 Targeting of ore rich in light-colored sphalerite, principally of orange and yellow colors, typically
848 formed in low-temperature stages of the mineralization process, may preliminarily constitute a
849 guideline in exploration for Ge in MVT deposits.

850 **Acknowledgements**

851 This study was economically supported by the Peruvian CONCYTEC-FONDECYT-World Bank
852 project 107-2018-FONDECYT-BM-IADT-AV managed through the PROCIENCIA agency. We
853 want to thank the staff of SIMSA - Unidad Minera San Vicente for the help and hospitality during
854 sampling tasks and the Minera Nexa Resources for providing samples from the Shalipayco
855 deposit. We appreciate the technical support by Xavier Llovet (CCiT-UB) during the acquisition
856 of EMPA data and by Pete Tollan (ETH) during the acquisition of LA-ICP-MS data. Finally, we
857 also would like to thank Alejandro Vargas (BIZALAB.SAC) for the SEM analyses. We are
858 grateful to Frank Melcher, Associate Editor Hartwig Frimmel, and Editor-in-Chief Bernd
859 Lehmann for their constructive comments which significantly improved the manuscript.

860 **Conflict of interest**

861 The authors declare no competing interest.

862 **References**

863 Awadh SM (2009) Iron content variations in sphalerite and their effects on reflectance and
864 internal reflections under reflected light. *Arab J Geosci* 2:139–142

865 Baby P, Calderón Y, Hurtado C, Louterbach M, Espurt N, Brusset S, Roddaz M, Brichau S,
866 Eude A, Calvès G (2019) The Peruvian Sub-Andean foreland basin system: structural
867 overview, geochronologic constraints, and unexplored plays. In: Zamora G, McClay KR,
868 Ramos VA (eds) *Memoir 117: Petroleum basins and hydrocarbon potential of the Andes of*
869 *Peru and Bolivia. American Association of Petroleum Geologists Special Volumes* 117:87–
870 116

871 Badoux V, Moritz R, Fontboté L (2001) The Mississippi Valley-type Zn-Pb deposit of San
872 Vicente, Central Peru: an Andean syntectonic deposit. *Proceedings of the Joint 6th Biennial*
873 *SGA-SEG Meeting, Mineral deposits at the beginning of the 21st Century, Krakow*, pp 191–
874 195

875 Bastian LM (2021) Fluid and metal sources of Zn-Pb sulfides of San Vicente, Peru. Ms.C.
876 Dissertation, ETH Zürich.

877 Bauer ME, Burisch M, Ostendorf J, Krause J, Frenzel M, Seifert T, Gutzmer J (2019) Trace
878 element geochemistry of sphalerite in contrasting hydrothermal fluid systems of the
879 Freiberg district, Germany: insights from LA-ICP-MS analysis, near-infrared light
880 microthermometry of sphalerite-hosted fluid inclusions, and sulfur isotope geochemistry.

881 Miner Deposita 54:237–262

882 Baumgartner RJ, Van Kranendonk MJ, Pagès A, Fiorentini ML, Wacey D, Ryan C (2020)
883 Accumulation of transition metals and metalloids in sulfidized stromatolites of the 3.48
884 billion–year–old Dresser Formation, Pilbara Craton. *Precambrian Res* 337:105534

885 Belissont R (2016) Germanium and related elements in sulphide minerals: crystal chemistry,
886 incorporation and isotope fractionation. Ph.D. Dissertation, Université de Lorraine.

887 Belissont R, Boiron MC, Luais B, Cathelineau M (2014) LA-ICP-MS analyses of minor and trace
888 elements and bulk Ge isotopes in zoned Ge-rich sphalerites from the Noailhac - Saint-
889 Salvy deposit (France): insights into incorporation mechanisms and ore deposition
890 processes. *Geochim Cosmochim Acta* 126:518–540

891 Belissont R, Muñoz M, Boiron MC, Luais B, Mathon O (2016) Distribution and oxidation state
892 of Ge, Cu and Fe in sphalerite by μ -XRF and K-edge μ -XANES: insights into Ge
893 incorporation, partitioning and isotopic fractionation. *Geochim Cosmochim Acta* 177:298–314

894 Benavides-Cáceres V (1999) Orogenic evolution of the Peruvian Andes: the Andean cycle. In:
895 Skinner BJ (ed) *Geology and Mineral Deposits of the Central Andes*. Society of Economic
896 Geologists Special Publication 7:61–107.

897 Benites D, Torró L, Vallance J, Laurent O, Valverde PE, Kouzmanov K, Chelle-Michou C,
898 Fontboté L (2021) Distribution of indium, germanium, gallium and other minor and trace
899 elements in polymetallic ores from a porphyry system: the Morococha District, Peru. *Ore*
900 *Geol Rev* 136, 104236

901 Benites D, Torró L, Vallance J, Laurent O, Quispe P, Rosas S, Uzieda MF, Holm-Denoma H,

902 Pianoski LS, Camprubí A, Colás V, Fernández-Baca A, Giraldo L, Chelle-Michou C, Sáez
903 J, Kouzmanov K, Fontboté L (2022) Geology, mineralogy, and cassiterite geochronology
904 of the Ayawilca Zn-Pb-Ag-In-Sn-Cu deposit, Pasco, Peru. *Miner Deposita* 57:481–507

905 Bente K, Wagner G, Lazar M, Lange U, Doering Th, Rao KV, Zehnder Th, Luck I, Lewerenz K-
906 J (1998) Thin films of semiconducting ZnS-CuInS₂ alloys, their characterization and use
907 for solar cells. In: Tomlinson RD, Hill AE, Pilkington RD (eds) Ternary and multinary
908 compounds: Proceedings, ICTMC-11, University of Salford, Institute of Physics
909 Conference Series Volume 152, 935–938

910 Bernstein LR (1985) Germanium: geochemistry and mineralogy. *Geochim Cosmochim Acta*
911 49:2409–2422

912 Berrospi-Rodríguez R, Fiestas J, Alvarado A, Leach D, Sempere T (2018) Role of Jurassic salt
913 tectonics in the structural shaping of MVT Pb-Zn deposits and hydrocarbon traps in Peru,
914 and implications for exploration. Abstracts of the SEG Conference, Colorado, #SP2.06

915 Bonnet J, Mosser-Ruck R, Caumon MC, Rouer O, Andre-Mayer AS, Cauzid J, Peiffert C (2016)
916 Trace element distribution (Cu, Ga, Ge, Cd, and Fe) in sphalerite from the Tennessee MVT
917 deposits, USA, by combined EMPA, LA-ICP-MS, Raman spectroscopy, and
918 crystallography. *Can Mineral* 54:1261–1284

919 Boussingault JB (1830) Analyse de la blende noire de Marmato, province de Popayán. *Ann*
920 *Chim Phys* 42:312–316

921 Bradbury JC (1961) Mineralogy and the question of zoning, Northwestern Illinois zinc-lead
922 district. *Econ Geol* 56:132–148

- 923 Bradley DC, Leach DL (2003) Tectonic controls of Mississippi Valley-type lead-zinc
924 mineralization in orogenic forelands. *Miner Deposita* 38:652–667
- 925 Capdevila R, Mégard F, Paredes J, Vidal P (1977) Le batholite de San Ramón, Cordillère
926 Orientale du Pérou central. *Geol Rundsch* 66:434–446
- 927 Carlotto V, Quispe J, Acosta H, Rodríguez R, Romero D, Cerpa L, Mamani M, Díaz-Martínez
928 E, Navarro P, Jaimes F (2009) Dominios geotectónicos y metalogénesis del Perú. *Boletín
929 de la Sociedad Geológica del Perú* 103:1–89
- 930 Carrillo E, Barragán R, Hurtado C, Calderón Y, Martín G, Marino E, Sarmiento L, Rivera A,
931 Fontboté L, Rosas S (2022) Sedimentary evolution of an Upper Triassic salt giant and a
932 synchronous carbonate unit between the Peruvian Andean Cordillera and the Brazilian
933 Amazonian foreland. *AAPG Bull* 107, *in press*. DOI 10.1306/08072221104
- 934 Cave B, Lilly R, Hong W (2020) The effect of co-crystallising sulphides and precipitation
935 mechanisms on sphalerite. *Geochemistry: a case study from the Hilton Zn-Pb (Ag) deposit,
936 Australia*. *Minerals* 10:797
- 937 Chew DM, Schaltegger U, Kosler J, Whitehouse MJ, Gutjahr M, Spikings RA, Mišković A (2007)
938 U-Pb geochronologic evidence for the evolution of the Gondwanan margin of the north-
939 central Andes. *Geol Soc Am Bull* 119:697–711
- 940 Chew DM, Pedemonte G, Corbett E (2016) Proto-Andean evolution of the Eastern Cordillera
941 of Peru. *Gondwana Res* 35:59–78
- 942 Chiaradia M, Fontboté L (2003) Separate lead isotope analyses of leachate and residue rock
943 fractions: implications for metal source tracing in ore deposit studies. *Miner Deposita*

- 944 38:185–195
- 945 Chirico R, Mondillo N, Boni M, Joachimski MM, Ambrosino M, Buret Y, Mormone A, Beteta
946 Leigh LEN, Huaman Flores W, Balassone G (2022) Genesis of the Florida Canyon
947 Nonsulfide Zn Ores (Northern Peru): New Insights Into the Supergene Mineralizing Events
948 of the Bongará District. *Econ Geol* 117:1339–1366
- 949 Çiftçi E (2009) Mercurian sphalerite from Akoluk deposit (Ordu, NE Turkey): Hg as a
950 cathodoluminescence activator. *Mineral Mag* 73:257–267
- 951 Ciobanu CL, Cook NJ, Utsunomiya S, Pring A, Green L (2011) Focussed ion beam—
952 transmission electron microscopy applications in ore mineralogy: Bridging micro- and
953 nanoscale observations. *Ore Geol Rev* 42:6–31
- 954 Cook NJ, Ciobanu CL, Pring A, Skinner W, Shimizu M, Danyushevsky L, Saini-Eidukat B,
955 Melcher F (2009) Trace and minor elements in sphalerite: a LA-ICPMS study. *Geochim
956 Cosmochim Ac* 73:4761–4791
- 957 Cook NJ, Etschmann B, Ciobanu CL, Geraki K, Howard DL, Williams T, Rae N, Pring A, Chen
958 G, Johannessen B, Brugger J (2015a) Distribution and substitution mechanism of Ge in a
959 Ge-(Fe)-bearing sphalerite. *Minerals* 5:117–132
- 960 Cook NJ, Etschmann B, Ciobanu CL, Howard D, Williams T, Rae N, Pring A, Geraki K, Chen
961 GR, Brugger J (2015b) Synchrotron XANES study of a Ge-(Fe)-bearing sphalerite.
962 *Minerals* 5:117–132
- 963 Craig JR, Vaughan DJ (1994) *Ore Microscopy and Ore Petrography*. John Wiley & Sons Ltd,
964 New York.
- 965 Dana ES (1892) *System of mineralogy*. John Wiley & Sons Ltd, New York.

- 966 Dávila D, Febres O, Fontboté L, Oldham L (2000) Exploración y geología del yacimiento San
967 Vicente. In: Yacimientos minerales peruanos. Instituto Ingenieros de Minas del Perú, 1,
968 305–328
- 969 Dávila D, Huyhua G, Flores C (2014) Estilo y geometría de mineralización MVT en la mina San
970 Vicente. Congreso Geológico Peruano, Resúmenes Extendidos, 4 p
- 971 de Oliveira SB, Leach DL, Juliani C, Monteiro LVS, Johnson CA (2019) The Zn–Pb
972 mineralization of Florida Canyon, an evaporite-related Mississippi Valley-type deposit in
973 the Bongará district, Northern Peru. *Econ Geol* 114:1621–1647
- 974 de Oliveira SB, Juliani C, Monteiro LVS, Tassinari CCG (2020) Structural control and timing of
975 evaporite-related Mississippi Valley-type Zn–Pb deposits in Pucará Group, Northern
976 Central Peru. *J S Am Earth Sci* 103:102736
- 977 de Oliveira SB, Johnson CA, Juliani C, Monteiro LVS, Leach DL, Caran MGN (2021) Geology
978 and genesis of the Shalipayco evaporite-related Mississippi Valley-type Zn–Pb deposit,
979 Central Peru: 3D geological modeling and C–O–S–Sr isotope constraints. *Miner Deposita*
980 56:1543–1563
- 981 Di Benedetto F, Bernardini GP, Costagliola P, Plant D, Vaughan DJ (2005) Compositional zoning
982 in sphalerite crystals. *Am Mineral* 90:1384–1392
- 983 European Commission (2020) Study on the EU's list of Critical Raw Materials (final report).
984 European Commission, Brussels, pp 1–158
- 985 Foley N, Jaskula B, Kimball B, Schulte F (2017) Gallium. In: Critical Mineral Resources of the
986 United States, Economic and Environmental Geology and Prospects for Future Supply,

- 987 U.S. Geological Survey, Virginia, pp 1–26
- 988 Fontboté L (1993) Self-organization fabrics in carbonate-hosted ore deposits: the example of
989 diagenetic crystallization rhythmites (DCRs). In: Fenoll Hach-Ali P, Torres-Ruiz J, Gervilla
990 F (eds) Current research in geology applied to ore deposits. Proceedings of the Second
991 Biennial SGA Meeting, Granada, pp 11–14
- 992 Fontboté L (2018) Ore deposits of the Central Andes. *Elements* 14:257–261
- 993 Fontboté L, Gorzawski H (1990) Genesis of the Mississippi Valley-type Zn-Pb deposit of San
994 Vicente, Central Peru; geologic and isotopic (Sr, O, C, S, Pb) evidence. *Econ Geol*
995 85:1402–1437
- 996 Fontboté L, Gunnesch KA, Baumann A (1990) Metal sources in stratabound ore deposits in the
997 Andes (Andean Cycle) - Lead isotopic constraints. In: Fontboté L, Amstutz GC, Cardozo
998 M, Cedillo E, Frutos J (eds) Stratabound ore deposits in the Andes. Special Publication 8
999 of the Society for Geology Applied to Mineral Deposits, Springer, Heidelberg, p. 759–773
- 1000 Fontboté L, Spangenberg J, Oldham L, Dávila D, Febres O (1995) The Mississippi Valley-type
1001 zinc-lead mine of San Vicente, Eastern Pucará basin, Peru. Extended Abstracts of the
1002 International Field Conference on Carbonate Hosted Lead-Zinc Deposits, St. Louis, p. 83–
1003 86
- 1004 Frenzel M, Hirsch T, Gutzmer J (2016) Gallium, germanium, indium, and other trace and minor
1005 elements in sphalerite as a function of deposit type — A meta -analysis. *Ore Geol Rev*
1006 76:52–78
- 1007 Gómez-Fernández F, Both RA, Mangas J, Arribas A (2000) Metallogenesis of Zn-Pb carbonate-

1008 hosted mineralization in the southeastern region of the Picos de Europa (Central Northern
1009 Spain) Province: geologic, fluid inclusion, and stable isotope studies. *Econ Geol* 95:19–40

1010 Guillong M, Hametner K, Reusser E, Wilson SA, Günther D (2005) Preliminary characterisation
1011 of new glass reference materials (GSA-1G, GSC-1G, GSD-1G and GSE-1G) by laser
1012 ablation-inductively coupled plasma-mass spectrometry using 193 nm, 213 nm and 266
1013 nm wavelengths. *Geostand Geoanal Res* 29:315–331

1014 Guillong M, Meier DL, Allan MM, Heinrich CA, Yardley BWD (2008) SILLS: a matlab-based
1015 program for the reduction of Laser Ablation ICP–MS data of homogeneous materials and
1016 inclusions. In: Sylvester P (ed) *Laser Ablation ICP-MS in the Earth Sciences: current
1017 practices and outstanding issues*. Mineralogical Association of Canada Short Course
1018 40:328–333

1019 Guillong M, Wotzlaw JF, Looser N, Laurent O (2020) New analytical and data evaluation
1020 protocols to improve the reliability of U-Pb LA-ICP-MS carbonate dating. *Geochronology*
1021 <https://doi.org/10.5194/gchron-2019-20>

1022 Gunnesch KA, Baumann A, Gunnesch M (1990) Lead isotope variations across the Central
1023 Peruvian Andes. *Econ Geol* 85:1384–1401

1024 Hofmann C, Henn U (1985) Green sphalerite from Zaire. *Journal of Gemmology* 19:416–418

1025 Höll R, Kling M, Schroll E (2007) Metallogeneses of germanium - a review. *Ore Geol Rev*
1026 30:145–180

1027 Hulse DE, Malhotra D, Mortimer S (2021) NI 43-101 Technical Report on Resources Florida
1028 Canyon Zinc Project, Amazonas Department, Peru. Gustavson Associates for Solitario

- 1029 Zinc Corp., 165 p
- 1030 Jenks WF (1951) Triassic to Tertiary stratigraphy near Cerro de Pasco, Peru. *Geol Soc Am Bull*
1031 62:202 – 220
- 1032 Jochum KP, Weis U, Stoll B, Kuzmin D, Yang Q, Raczek I, Jacob DE, Stracke A, Birbaum K,
1033 Frick DA, Günther D,ENZWEILER J (2011) Determination of reference values for NIST SRM
1034 610-617 glasses following ISO guidelines. *Geostand Geoanal Res* 35:397–429
- 1035 Johan Z (1988) Indium and germanium in the structure of sphalerite: an example of coupled
1036 substitution with copper. *Miner Petrol* 39:211–229
- 1037 Jolly JL, Heyl AV (1964) Mineral paragenesis and zoning in the Central Kentucky Mineral
1038 district. *Econ Geol* 59:596–624
- 1039 Katsev S, L'Heureux I, Fowler A (2001) Mechanism and duration of banding in Mississippi
1040 Valley-type sphalerite. *Geophys Res Lett* 28:4643–4646
- 1041 Kelka U, Veveakis M, Koehn D, Beaudoin N (2017) Zebra rocks: compaction waves create ore
1042 deposits. *Sci Rep* 7:14260
- 1043 Kelley KD, Leach DL, Johnson CA, Clark JL, Fayek M, Slack JF, Anderson VM, Ayuso RA,
1044 Ridley WI (2004) Textural, compositional, and sulfur isotope variations of sulfide minerals
1045 in the Red Dog Zn-Pb-Ag deposits, Brooks Range, Alaska: implications for ore formation.
1046 *Econ Geol* 99:1509–1532
- 1047 Knorsch M, Nadoll P, Klemd R (2020) Trace elements and textures of hydrothermal sphalerite
1048 and pyrite in Upper Permian (Zechstein) carbonates of the North German Basin. *J*
1049 *Geochem Explor* 209:106416

- 1050 Kontak DJ, Clark AH, Farrar E, Strong DF (1985) The rift associated Permo-Triassic
1051 magmatism of the Eastern Cordillera: a precursor of the Andean orogeny. In: Atherton WS,
1052 Pitcher MP, Cobbing EJ, Beckinsale RD (eds) Magmatism at a plate edge. The Peruvian
1053 Andes, Wiley, New York, pp 36–44
- 1054 Lancelot JR, Laubacher G, Marocco R, Renaud U (1978) U/Pb radiochronology of two granitic
1055 plutons from the Eastern Cordillera (Peru) - extent of Permian magmatic activity and
1056 consequences. *Geol Rundsch* 67:236–243
- 1057 Leach DL, Sangster DF, Kelley KD, Large RR, Garven G, Allen CR, Gutzmer J, Walters S
1058 (2005) Sediment-hosted lead-zinc deposits: a global perspective. In: Hedenquist JW,
1059 Thompson JFH, Goldfarb RJ, Richards, JP (eds) One Hundredth Anniversary Volume,
1060 Society of Economic Geologists, Littleton, pp 561–607
- 1061 Leach DL, Taylor RD, Fey DL, Diehl SF, Saltus RW (2010) A deposit model for Mississippi
1062 Valley-type lead-zinc ores. In: Chapter A of mineral deposit models for resource
1063 assessment. U.S Geological Survey Scientific Investigations Report 2010–5070–A.
1064 <https://doi.org/10.3133/sir20105070A>
- 1065 Li M, Barnes HL (2019) Orbitally forced sphalerite growth in the Upper Mississippi Valley district.
1066 *Geochem Perspect Lett* 12:18–22
- 1067 Liu W, Mei Y, Etschmann B, Glenn M, MacRae C, Spinks SC, Ryan CG, Brugger J, Paterson
1068 DJ (2022) Germanium speciation in experimental and natural sphalerite: implications for
1069 critical metal enrichment in hydrothermal Zn-Pb ores. *Geochim Cosmochim Acta*, *in press*
1070 <https://doi.org/10.1016/j.gca.2022.11.031>
- 1071 Loughman DL, Hallam A (1982) A facies analysis of the Pucará Group (Norian to Toarcian

- 1072 carbonates, organic-rich shale and phosphate) of Central and Northern Peru. *Sediment*
1073 *Geol* 32:161–194
- 1074 Luo K, Cugerone A, Zhou MF, Zhou JX, Sun GT, Xu J, He KJ, Lu MD (2022) Germanium
1075 enrichment in sphalerite with acicular and euhedral textures: an example from the
1076 Zhulingou carbonate-hosted Zn(-Ge) deposit, South China. *Miner Deposita* 57:1343–1365
- 1077 McLaughlin DH (1924) *Geology and physiography of the Peruvian Cordillera*, Departments of
1078 Junin and Lima. *Geol Soc Am Bull* 35:591–632
- 1079 Mégard F (1978) *Etude géologique des Andes du Pérou Central*, contribution à l'étude
1080 géologique des Andes. Office de la Recherche Scientifique et Technique. Institut français
1081 d'études andines, Paris, 310 p
- 1082 Melcher F, Buchholz P (2014) Germanium. In: Gunn G (ed) *Critical Metals Handbook*, John
1083 Wiley & Sons, Ltd., Chichester, pp 177–203
- 1084 Merino E, Canals A (2011) Self-accelerating dolomite-for-calcite replacement: self-organized
1085 dynamics of burial dolomitization and associated mineralization. *Am J Sci* 311:573–607
- 1086 Möller P, Dulski P (1996) Germanium and gallium distribution in sphalerite: a key to the genesis
1087 of sediment-hosted sulphide mineralizations. *Zeitschrift für Geologische Wissenschaften*
1088 24:527–538
- 1089 Mondillo N, Arfè G, Boni M, Balassone G, Boyce A, Joachimski M, Kang JS, Villa IM (2018a)
1090 The Cristal Zinc prospect (Amazonas region, Northern Peru). Part I: new insights on the
1091 sulfide mineralization in the Bongará province. *Ore Geol Rev* 94:261–276
- 1092 Mondillo N, Arfè G, Herrington R, Boni M, Wilkinson C, Mormone A (2018b) Germanium

- 1093 enrichment in supergene settings: evidence from the Cristal nonsulfide Zn prospect,
1094 Bongará district, Northern Peru. *Miner Deposita* 53:155–169
- 1095 Moritz R, Fontboté L, Spangenberg J, Rosas S, Sharp Z, Fontignie D (1996) Sr, C and O isotope
1096 systematics in the Pucará basin, Central Peru. *Miner Deposita* 31:147–162
- 1097 Moskalyk RR (2003) Gallium: the backbone of the electronic industry. *Miner Eng* 16:921-929
- 1098 Muñoz C, Farfán C, López G, Rosas S (2000) Vulcanismo asociado a los carbonatos del Grupo
1099 Pucará (Triásico Superior – Liásico) en el área de Shalipayco, Junín – Perú Central.
1100 Resúmenes X Congreso Peruano de Geología, Sociedad Geológica del Perú, Lima,
1101 Publicación Especial 2:42
- 1102 Noble DC, Silberman ML, Mégard F, Bowman HP (1978) Comendite (peralkaline rhyolite) and
1103 basalt in the Mitu Group, Peru: evidence for Permian-Triassic lithospheric extension in the
1104 Central Andes. *Journal of Research US Geological Survey* 6:453–457
- 1105 Oldham L, Dávila D, Flores W, Mamani W, Minaya J, Cano P (2017) Reporte annual de
1106 exploraciones. Proyecto Shalipayco. Proprietary Report
- 1107 Ostendorf J, Henjes-Kunst F, Mondillo N, Boni M, Schneider J, Gutzmer J (2015) Formation of
1108 Mississippi Valley-type deposits linked to hydrocarbon generation in extensional tectonic
1109 settings: Evidence from the Jabali Zn-Pb-(Ag) deposit (Yemen). *Geology* 43:1055–1058
- 1110 Ostendorf J, Henjes-Kunst F, Schneider J, Melcher F, Gutzmer J (2017) Genesis of the
1111 carbonate-hosted Tres Marias Zn-Pb-(Ge) deposit, Mexico: constraints from Rb-Sr
1112 sphalerite geochronology and Pb isotopes. *Econ Geol* 112:1075–1087
- 1113 Palache C, Berman H, Frondel C (1944) The system of mineralogy of James Dwight Dana and

- 1114 Edward Salisbury Dana Yale University 1837-1892, Volume I: Elements, Sulfides,
1115 Sulfosalts, Oxides. John Wiley and Sons, New York
- 1116 Paradis S (2015) Indium, germanium and gallium in volcanic- and sediment-hosted base-metal
1117 sulphide deposits. In: Simandl GJ, Neetz M (eds) Symposium on Strategic and Critical
1118 Materials Proceedings. British Columbia. British Columbia Geological Survey Paper,
1119 Victoria, 2015-3:23–29
- 1120 Paton C, Hellstrom J, Paul B, Woodhead J, Hergt J (2011) Lolite: Freeware for the visualisation
1121 and processing of mass spectrometric data. *J Anal At Spectrom* 26:2508–2518
- 1122 Pósfai M, Dódony I, Soós M (1988) Stacking disorder in the ZnS from Gyöngyösoroszi,
1123 Hungary. *Neues Jb Miner Monat* 10:438–445
- 1124 Rager H, Amthauer G, Bernroider M, Schürmann K (1996) Colour, crystal chemistry, and
1125 mineral association of a green sphalerite from Steinperf, Dill syncline, FRG. *Eur J Mineral*
1126 8:1191–1198
- 1127 Ramdohr P (1980) *The ore minerals and their intergrowths*. Pergamon Press, Oxford
- 1128 Ramírez J, Torró L, Quispe P, Benites D, Vallance J, Rosas S, Guzmán L, Fernández-Baca A,
1129 Spangenberg JE, Vennemann T, Chiaradia M, Kouzmanov K, Fontboté L (2022) Isotopic
1130 compositions of sulfides (S) and anhydrite (S, O, Sr) from the Ayawilca polymetallic
1131 deposit, Pasco, Peru. In: Christie AB (ed) *Proceedings of the 16th SGA Biennial Meeting*
1132 1:336–339
- 1133 Ritterbush KA, Rosas S, Corsetti FA, Bottjer DJ, West AJ (2015) Andean sponges reveal long-
1134 term benthic ecosystem shifts following the end-Triassic mass extinction. *Palaeogeogr*

- 1135 Palaeocl 420:193–209
- 1136 Robson D, Carlsson J, Altman K, Theben S (2017) NI 43-101 Technical report on the
1137 preliminary economic assessment of the Shalipayco project, Junín Region, Peru. RPA,
1138 Toronto, 194 pp
- 1139 Roedder E, Dwornik EJ (1968) Sphalerite color banding. Lack of correlation with iron content,
1140 Pine Point, Northwest Territories, Canada. Am Mineral 53:1523–1529
- 1141 Rosas S (2016) Profundización sedimentaria solo en la parte de la cuenca Pucará (Perú
1142 Central) durante el Hetangiano Sinemuriano. Resúmenes del XVIII Congreso Peruano de
1143 Geología, Sociedad Geológica del Perú, Lima, p 1–4
- 1144 Rosas S, Fontboté L (1995) Evolución sedimentológica del Grupo Pucará (Triásico Superior –
1145 Jurásico Inferior) en un perfil SW-NE en el Centro del Perú. Volumen Jubilar Alberto
1146 Benavides, Sociedad Geológica del Perú, Lima, p 279–309
- 1147 Rosas S, Fontboté L, Tankard A (2007) Tectonic evolution and paleogeography of the Mesozoic
1148 Pucará basin, Central Peru. J S A Earth Sci 24:1–24
- 1149 Saini-Eidukat B, Melcher F, Lodziak J (2009) Zinc-germanium ores of the Tres Marias mine,
1150 Chihuahua, Mexico. Miner Deposita 44:363–370
- 1151 Saintilan NJ, Spangenberg JE, Chiaradia M, Chelle-Michou C, Stephens MB, Fontboté L (2019)
1152 Petroleum as source and carrier of metals in epigenetic sediment-hosted mineralization.
1153 Sci Rep 9:1–8
- 1154 Saintilan NJ, Sproson AD, Selby D, Rottier B, Casanova V, Creaser RA, Kouzmanov K,
1155 Fontboté L, Piecha M, Gereke M, Zambito IV JJ (2021) Osmium isotopic constraints on

- 1156 sulphide formation in the epithermal environment of magmatic-hydrothermal mineral
1157 deposits. *Chem Geol* 564:120053
- 1158 Sanabria R, García-Álvarez JR (2005) Les sphalérites d'Aliva, Picos de Europa (Espagne). *Le*
1159 *Règne Minéral* 63:6–27
- 1160 Sangster DF (1995) Mississippi Valley-type lead-zinc. In: Eckstrand OR, Sinclair WD, Thorpe
1161 RI (eds) *Geology of Canadian Mineral Deposit Types*. Geological Survey of Canada,
1162 *Geology of Canada* 8:253–261
- 1163 Sapalski C, Gómez F (1992) Estudio de la esfalerita de la mina de Ávila, Santander. *Boletín*
1164 *del Instituto Gemológico Español* 34:28–39
- 1165 Schaltegger U, Guex J, Bartolini A, Schoene B, Ovtcharova M (2008) Precise U–Pb age
1166 constraints for end-Triassic mass extinction, its correlation to volcanism and Hettangian
1167 post-extinction recovery. *Earth Planet Sc Lett* 267:266–275
- 1168 Schutfort EG (2001) The genesis of the San Vicente lead-zinc rhythmites deposit, Peru: a
1169 petrologic, geochemical, and sulfur isotope study. Dissertation, Oregon State University
- 1170 Scott SD, Barnes HL (1972) Sphalerite-wurtzite equilibria and stoichiometry. *Geochim*
1171 *Cosmochim Ac* 36:1275–1295
- 1172 Sempere TPA, Cotrina J (2018) An overlooked giant salt basin in Peru. Proceedings of the 9th
1173 INGEPET, Lima, paper GEO-EX-TS-10-N, 18 pp
- 1174 Shanks III WCP, Kimball BE, Tolcin AC, Guberman DE (2017) Germanium and indium. In:
1175 Schulz KJ, DeYoung JH, Seal II RR, Bradley DC (eds) *Critical mineral resources of the*
1176 *United States—Economic and environmental geology and prospects for future supply: US*

- 1177 Geological Survey Professional Paper, 1802 I1–I27
- 1178 SIMSA (2021) Compañía Minera San Ignacio de Morococha S.A.A.: Memoria Annual 2021,
1179 Lima. https://www.simsa.com.pe/assets/pdf/Memoria_Anual_2021.pdf. Accessed 30 May
1180 2022
- 1181 Slack GA, Ham FS, Chrenko RM (1966) Optical absorption of tetrahedral Fe²⁺ (3d⁶) in cubic
1182 ZnS, CdTe, and MgAl₂O₄. Phys Rev 152:376–402
- 1183 Slack GA, Roberts S, Ham FS (1967) Far-infrared optical absorption of Fe²⁺ in ZnS. Phys Rev
1184 155:170–177
- 1185 Sokol EV, Kokh SN, Seryotkin YV, Deviatiiarova AS, Goryainov SV, Sharygin VV, Khoury HN,
1186 Karmanov NS, Danilovsky VA, Artemyev DA (2020) Ultrahigh-temperature sphalerite from
1187 Zn-Cd-Se-Rich combustion metamorphic marbles, Daba Complex, Central Jordan:
1188 Paragenesis, chemistry, and structure. Minerals 10:822
- 1189 Spangenberg JE (1995) Geochemical (elemental and isotopic) constraints on the genesis of
1190 the Mississippi Valley-type zinc-lead deposit of San Vicente, Central Peru. Dissertation,
1191 Université de Genève
- 1192 Spangenberg JE, Macko SA (1998) Organic geochemistry of the San Vicente zinc-lead district,
1193 eastern Pucará Basin, Peru. Chem Geol 146:1–23
- 1194 Spangenberg JE, Fontboté L, Sharp ZD, Hunziker J (1996) Carbon and oxygen isotope study
1195 of hydrothermal carbonates in the zinc-lead deposits of the San Vicente district, Central
1196 Peru: a quantitative modeling on mixing processes and CO₂ degassing. Chem Geol
1197 133:289–315

- 1198 Spangenberg JE, Fontboté L, Macko SA (1999) An evaluation of the inorganic and organic
1199 geochemistry of the San Vicente Mississippi Valley-type zinc-lead district, Central Peru;
1200 implications for ore fluid composition, mixing processes, and sulfate reduction. *Econ Geol*
1201 94:1067–1092
- 1202 Spikings R, Reitsma MJ, Boekhout F, Mišković A, Ulianov A, Chiaradia M, Gerdes A,
1203 Schaltegger U (2016) Characterisation of Triassic rifting in Peru and implications for the
1204 early disassembly of western Pangaea. *Gondwana Res* 35:124–143
- 1205 Šrot V, Rečnik A, Scheu C, Šturm S, Mirtič B (2003) Stacking faults and twin boundaries in
1206 sphalerite crystals from the Trepča mines in Kosovo. *Am Mineral* 88:1809–1816
- 1207 Stipetich S, Vallance J, Torró L, Rosas S, Benites D, Valverde P, Zorrilla A, Valencia E, Zárate
1208 J, Díaz R, Huamantalla J, Spangenberg JE, Vennemann T, Kouzmanov K, Chiaradia M,
1209 Fontboté L (2022) Role of massive anhydrite bodies in the Cordilleran-type polymetallic
1210 mineralization of Morococha district, Peru: 3D geological modeling and Sr-S-O isotope
1211 constraints. In: Christie AB (ed) *Proceedings of the 16th SGA Biennial Meeting* 1:372–375
- 1212 Szekely TS, Grose LT (1972) Stratigraphy of the carbonate, black shale, and phosphate of the
1213 Pucará Group (Upper Triassic-Lower Jurassic), Central Andes, Peru. *Geol Soc Am Bull*
1214 83:407–428
- 1215 Ujaczki E, Courtney R, Cusack P, Krishna Chinnam R, Clifford S, Curtin T, O'Donoghue L (2019)
1216 Recovery of gallium from bauxite residue using combined oxalic acid leaching with
1217 adsorption onto zeolite HY. *J Sustain Metall* 5:262–274
- 1218 Wei C, Ye L, Hu Y, Danyushevskiy L, Li Z, Huang Z (2019) Distribution and occurrence of Ge
1219 and related trace elements in sphalerite from the Lehong carbonate-hosted Zn-Pb deposit,

- 1220 Northeastern Yunnan, China: insights from SEM and LA-ICP-MS studies. *Ore Geol Rev*
1221 115:103175
- 1222 Wei C, Ye L, Hu Y, Huang Z, Danyushevsky L, Wang H (2021) LA-ICP-MS analyses of trace
1223 elements in base metal sulfides from carbonate-hosted Zn-Pb deposits, South China: A
1224 case study of the Maoping deposit. *Ore Geol Rev* 130:103945
- 1225 Wilkinson JJ (2014) Sediment-hosted zinc-lead mineralization. In: Holland H, Turekian K (eds)
1226 *Treatise on Geochemistry* 13:219–249
- 1227 Wilson SA, Ridley WI, Koenig AE (2002) Development of sulfide calibration standards for the
1228 laser ablation inductively-coupled plasma mass spectrometry technique. *J Anal Atom*
1229 *Spectrom* 17:406–409
- 1230 Wood GD, Groves JR, Wahlman GP, Brenckle PL, Alemán AM (2002) The paleogeographic
1231 and biostratigraphic significance of fusulinacean and smaller foraminifers, and
1232 palynomorphs from the Copacabana Formation (Pennsylvanian-Permian), Madre de Dios
1233 Basin, Peru. In: Hills LV, Henderson CM, Bamber EW (eds) *Carboniferous and Permian of*
1234 *the World*. Canadian Society of Petroleum Geologist, *Memoirs* 19:630–664
- 1235 Xu J, Ciobanu CL, Cook NJ, Slattery A, Li X, Kontonikas-Charos A (2022) Phase relationships
1236 in the system ZnS-CuInS₂: Insights from a nanoscale study of indium-bearing sphalerite.
1237 *Am Mineral*, <https://doi.org/10.2138/am-2020-7488>
- 1238 Ye L, Li Z, Hu Y, Huang Z, Zhou J, Fan H, Danyushevsky LV (2016) Trace elements in sulfide
1239 from the Tianbaoshan Pb-Zn deposit, Sichuan province, China: a LA-ICPMS study. *Acta*
1240 *Petrol Sin* 32:3377–3393

1241 Ye L, Cook NJ, Ciobanu CL, Yuping L, Qian Z, Tiegeng L, Wei G, Yulong Y, Danyushevskiy L
1242 (2011) Trace and minor elements in sphalerite from base metal deposits in South China: A
1243 LA-ICPMS study. *Ore Geol Rev* 39:188–217

1244 Yuan B, Zhang C, Yu H, Yang Y, Zhao Y, Zhu C, Ding Q, Zhou Y, Yang J, Xu Y (2018) Element
1245 enrichment characteristics: insights from element geochemistry of sphalerite in Daliangzi
1246 Pb-Zn deposit, Sichuan, Southwest China. *J Geochem Explor* 186:187–201

1247 **Figure captions**

1248 **Fig. 1** Morphostructural units of Peru (modified from [Benavides-Cáceres 1999](#)), including the
1249 location of MVT deposits/districts (yellow stars) in Peru. Topography base image taken from
1250 JPL-NASA ©

1251 **Fig. 2** Geological map of the San Vicente deposit. Modified from [Dávila et al. \(2000\)](#).
1252 Geochronology of igneous rocks from by [Capdevila et al. \(1977\)](#), [Lancelot et al. \(1978\)](#),
1253 [Gunnesch et al. \(1990\)](#), and [Chew et al. \(2007, 2016\)](#); see text for details. WSD: white sparry
1254 dolomite

1255 **Fig. 3** Hand-sample photographs showing different textures in ore samples from the San
1256 Vicente deposit. A) Rock with zebra-type texture consisting of bands of dark replacement
1257 dolomite + black sphalerite overgrown by reddish-brown and yellowish-brown sphalerite
1258 bands and white sparry dolomite 1. White sparry dolomite 1 cuts also the former bands
1259 (sample 2019-SV-02). B) Dark replacement dolomite + black sphalerite overgrown by
1260 reddish-brown and yellowish-brown sphalerite, followed by white sparry dolomite 1. Galena
1261 and white sparry dolomite 1 fill the remaining space (sample 2019-SV-11). C) Relictic dark
1262 replacement dolomite intergrown with black sphalerite, and reddish-brown and yellowish-

1263 brown sphalerite overgrowths replaced and cemented by white sparry dolomite 1 (sample
1264 2019-SV-12). D) Colloform reddish-brown sphalerite and galena overgrown by yellowish-
1265 brown and yellow sphalerite and white sparry dolomite 1. Note also veinlets of galena
1266 crosscutting the white sparry dolomite 1 cement (sample 2019-SV-01). E) Reddish-brown and
1267 yellowish-brown sphalerite colloform bands overgrown by first-step yellow sphalerite; clasts
1268 have been rotated and cemented by white sparry dolomite 1 (sample 2019-SV-03). F) Detail
1269 of a breccia in a steep crosscutting vein with partially dissolved and rotated dark replacement
1270 dolomite clasts mainly cemented by white sparry dolomite 1 and, postdating it, second-step
1271 orange and yellow sphalerite. G) Dark replacement dolomite replaced by second-step orange,
1272 yellow, and white sphalerite with cement of white sparry dolomite 2 (sample 2019-SV-13). H)
1273 Dark replacement dolomite replaced by second-step orange and yellow sphalerite (sample
1274 2019-SV-14). I) Black sphalerite cut by veinlets filled with white sparry dolomite 1 that in turn
1275 are cut by thin veinlets of white sphalerite (sample 2019-SV-05). **Abbreviations:** **DRD:** dark
1276 replacement dolomite; **gn:** galena; **mc:** marcasite; **py:** pyrite; **sl_{1b}:** first-step black sphalerite;
1277 **sl_{1rb}:** first-step reddish-brown sphalerite; **sl_{1yb}:** first-step yellowish-brown sphalerite; **sl_{1y}:** first-
1278 step yellow sphalerite; **sl_{2o}:** second-step orange sphalerite; **sl_{2y}:** second-step yellow
1279 sphalerite; **sl_{2w}:** second-step white sphalerite; **WSD₁:** white sparry dolomite 1; **WSD₂:** white
1280 sparry dolomite 2

1281 **Fig. 4** Photomicrographs of polished sections taken with reflected light without analyzer (PPL)
1282 and in crossed polars (XPL) showing textures of ore samples from the Saint Vincent deposit.
1283 A) Anhedral black sphalerite intergrown with fine-grained dark replacement dolomite. Veinlets
1284 are lined with white sparry dolomite 1 and 2. Calcite fills cracks and other voids. Black sphalerite
1285 is overgrown by white sphalerite. B) Subhedral crystals of reddish-brown sphalerite with
1286 gradation to first step yellow sphalerite. C) Cracked and partly dissolved black and yellowish-

1287 brown sphalerite cemented by white sparry dolomite 1 and cut by white sparry dolomite 2 and
1288 calcite. D) Anhedral to subhedral orange, yellow and white sphalerite with quartz and white
1289 sparry dolomite 2 and smithsonite. E) Anhedral yellow sphalerite with white sparry dolomite 2
1290 and calcite as microfractures and open space-filling. Galena occurs in microfractures across
1291 sphalerite. F) Aggregates of white sparry dolomite 1 and 2 and calcite cut by second-step white
1292 to pale-green sphalerite irregular vein. Black sphalerite relicts together with minute pyrite and
1293 galena grains are observed too. G) Dark replacement dolomite with interstitial pyrite and
1294 marcasite cemented by anhedral yellow sphalerite and white sparry dolomite 2. H) Anhedral
1295 orange sphalerite overgrown by yellow and white sphalerite, with white sparry dolomite 2 filling
1296 interstitial space. I) Anhedral reddish-brown and yellowish-brown sphalerite, with minute
1297 subhedral pyrite grains along microfractures. Galena and white sparry dolomite 2 occupy
1298 interstitial positions. **Abbreviations:** **cc:** calcite; **DRD:** dark replacement dolomite; **gn:** galena;
1299 **mc:** marcasite; **py:** pyrite; **qtz:** quartz; **sl_{1b}:** first-step black sphalerite; **sl_{1rb}:** first-step reddish-
1300 brown sphalerite; **sl_{1yb}:** first-step yellowish-brown sphalerite; **sl_{1y}:** first-step yellow sphalerite;
1301 **sl_{2o}:** second-step orange sphalerite; **sl_{2y}:** second-step yellow sphalerite; **sl_{2w}:** second-step white
1302 sphalerite; **smt:** smithsonite; **WSD₁:** white sparry dolomite 1; **WSD₂:** white sparry dolomite 2

1303 **Fig. 5** Paragenetic sequence of the San Vicente deposit based on the studied samples and
1304 [Fontboté and Gorzawski \(1990\)](#). Thick bars indicate higher abundance and dashed lines, lesser
1305 abundance. The color of the bars corresponds to the color of the different sphalerite types.

1306 **Abbreviations:** **DRD:** dark replacement dolomite; **sl:** sphalerite; **WSD:** white sparry dolomite

1307 **Fig. 6** Photomicrographs of polished sections taken with reflected light without analyzer (A,
1308 C, E, G, I, and K) and in crossed polars (B, D, F, H, J, and L) showing textures of ore samples
1309 from the Shalipayco deposit. A-B; C-D) Fine grained calcite with quartz, subhedral barite and

1310 dolomite 1 with cavities filled by pyrite and black sphalerite. Small prismatic crystals of
1311 marcasite on borders of black sphalerite are also observed. E-F) Prismatic barite crystals with
1312 inclusions of framboidal pyrite with aggregates of reddish-brown and yellowish-brown
1313 sphalerite in spaces between the barite lathes. G-H) Anhedronal grains of black, reddish-brown,
1314 yellowish-brown, yellow, and white sphalerite cut by dolomite 2. Pyrite inclusions in both
1315 sphalerite and dolomite 2 are observed I-J) Anhedronal yellowish-brown to yellow sphalerite
1316 crystals with interstitial dolomite 2 and galena. K-L) Anhedronal yellow and white sphalerite with
1317 dolomite 2. **Abbreviations:** **bar:** barite; **cc:** calcite; **dol₁:** dolomite 1; **dol₂:** dolomite 2; **gn:**
1318 galena; **mc:** marcasite; **py:** pyrite; **qtz:** quartz; **sl_{bl}:** black sphalerite; **sl_{rb}:** reddish-brown
1319 sphalerite; **sl_{yb}:** yellowish-brown sphalerite; **sl_y:** yellow sphalerite; **sl_w:** white sphalerite

1320 **Fig. 7** Paragenetic sequence of the Shalipayco deposit after [de Oliveira et al. \(2021\)](#). Thick
1321 bars indicate higher abundance and dashed lines, lesser abundances. The color of the bars
1322 corresponds to the color of the different sphalerite types. **Abbreviations:** **dol₁:** dolomite 1;
1323 **dol₂:** dolomite 2; **sl:** sphalerite

1324 **Fig. 8** Boxplot of LA-ICP-MS data for selected minor and trace elements in sphalerite from the
1325 San Vicente, Shalipayco, and Cristal deposits: a) iron, b) cadmium, c) manganese, d) copper,
1326 e) silver, f) tin, g) mercury, h) germanium, i) gallium, and j) indium. Analyses are plotted in
1327 parts per million (ppm) on a vertical logarithmic scale. The maximum, median, and minimum
1328 concentrations are indicated, as well as the number of analyses above the detection limit for
1329 each element (displayed up or below the boxes). Analyses with “spiky profiles” in Table S2,
1330 attributed to inclusions, are not plotted. Data for the Cristal deposit are from [Mondillo et al.](#)
1331 [\(2018b\)](#)

1332 **Fig. 9** Composition of reflected light (A-D) and HAADF-STEM and TEM-EDS elemental maps
1333 (A1 to D3) acquired for the four thin foils analyzed in this study. Dashed-line rectangles are the
1334 selected areas for HRTEM and SAED analysis shown in [Figure 12](#)

1335 **Fig. 10** Nanostructure of selected areas of the analyzed thin foils on sphalerite from the San
1336 Vicente deposit. A-D) thin foil #1 (sl_{1bl} and sl_{2w}), E-H) thin foil #2 (sl_{2y}), I-L) thin foil #3 (sl_{2o}), and
1337 M-P) thin foil #4 (sl_{2y} and sl_{2w}). Images A, C, E, and I are HAADF-STEM images, whereas B,
1338 G, J, N, and P show SAED with corresponding measured d-spacing. The HRTEM images are
1339 provided in D, F, H, K, L, M, and O

1340 **Fig. 11** Binary correlation plots for trace elements in sphalerite from San Vicente, Shalipayco,
1341 and Cristal deposits. Data for the Cristal deposit are from [Mondillo et al. \(2018b\)](#)

1342 **Fig. 12** Mean crystallization temperatures and 2 sigma error bars for the different sphalerite
1343 types analyzed in Peruvian MVT deposits calculated with the GGIMFis geothermometer of
1344 [Frenzel et al. \(2016\)](#). Legend as in [Fig. 11](#). A crystallization temperature for white sphalerite
1345 from the San Vicente deposit (sl_{2w}) could not be calculated since Fe contents are
1346 systematically <d.l. Data from the Cristal deposit are from [Mondillo et al. \(2018b\)](#)

1347 **Table captions**

1348 **Table 1** Summary of element contents in sphalerite from the San Vicente, Shalipayco, and
1349 Cristal deposits

1350 **Table 2** Formation temperature ($^{\circ}\text{C}$) of sphalerite according to the GGIMFis geothermometer
1351 of [Frenzel et al. \(2016\)](#)

1352 **Electronic Supplementary Material (ESM)**

1353 **Fig. S1** Hand-sample photographs showing different textures in samples from the Chilpes
1354 prospect. A-B) Sphalerite intergrown with white sparry dolomite. C) Sphalerite in massive
1355 pyrite layers. **Abbreviations:** **py:** pyrite; **sl_{rb}:** reddish-brown sphalerite; **sl_{yb}:** yellowish-brown
1356 sphalerite; **sl_o:** orange sphalerite; **sl_{2y}:** yellow sphalerite; **WSD:** white sparry dolomite.

1357 **Fig. S2** Photomicrographs of polished sections taken with reflected light without analyzer (A,
1358 C, E, G, I, and K) and in crossed polars (B, D, F, H, J, and L) showing textures of sphalerite-
1359 rich samples from the Chilpes prospect. A-B) Anhedral, porous reddish-brown sphalerite
1360 cemented by white sparry dolomite. Minute, roundish pyrite grains appear scattered in
1361 sphalerite and dolomite. C-D) Reddish-brown sphalerite cut by veinlets lined with white sparry
1362 dolomite. Minute, roundish pyrite grains appear scattered within sphalerite. E-F) Yellowish-
1363 brown sphalerite grain. G-H) Galena and orange sphalerite grains cemented by white sparry
1364 dolomite. I-J) Subhedral galena and anhedral orange sphalerite grains cemented by white
1365 sparry dolomite K-L) Yellow sphalerite grains cemented by white sparry dolomite. The circular
1366 structure in the bottom-center of the image is probably a ghost of an ooid. **Abbreviations:**
1367 **gn:** galena; **py:** pyrite; **sl_{rb}:** reddish-brown sphalerite; **sl_{yb}:** yellowish-brown sphalerite; **sl_o:**
1368 orange sphalerite; **sl_{2y}:** yellow sphalerite; **WSD:** white sparry dolomite.

1369 **Fig. S3** Photomicrographs of polished sections taken with reflected light without analyzer (A,
1370 C, and E) and in crossed polars (B, D, and F) showing textures of sphalerite-rich samples
1371 from the Huacrash prospect. In all photomicrographs, anhedral sphalerite showing brownish-
1372 orange internal reflections is cemented by white sparry dolomite. The "dirty" appearance of
1373 the sphalerite is due to not identified microinclusions. **Abbreviations:** **gn:** galena; **sl_{rb}:**
1374 brownish-orange sphalerite; **WSD:** white sparry dolomite.

1375 **Fig. S4** Whole mount optical-CL photograph of a sphalerite-bearing sample from the Chilpes
1376 prospect (sample FSV50). Sphalerite in this mount is orange in color and show marked
1377 oscillatory and sector zoning. **Abbreviations:** **sl_o**: orange sphalerite; **WSD**: white sparry
1378 dolomite.

1379 **Fig. S5** Binary Fe vs Zn correlation plot for analyzed sphalerite from the San Vicente deposit
1380 and data for the Cristal deposit provided by [Mondillo et al. \(2018b\)](#).

1381 **Table S1** List of samples and their location.

1382 **Table S2** Representative EMPA analyses of sphalerite. Structural formulas of sphalerite are
1383 normalized to S = 1.

1384 **Table S3** LA-ICP-MS trace element analyses on sphalerite- Metadata.

1385 **Table S4** LA-ICP-MS trace element analyses on sphalerite and reference materials.

Table 1

Ore-body/vein	Sphalerite type	Zn (wt%)	Fe (wt%)	Fe (ppm)	Mn (ppm)	Cd (ppm)	In (ppm)	Ge (ppm)	Ga (ppm)	Cu (ppm)	Ag (ppm)	Hg (ppm)	Tl (ppm)	As (ppm)	
San Vicente district (San Vicente + Chilpes + Huacrash)	All analyses (n = 357)	MIN.	-	-	B.D.L.	B.D.L.	185	B.D.L.	B.D.L.	B.D.L.	1.1	1.3	B.D.L.	B.D.L.	
		MAX.	-	-	43,271	1,161	16,422	92	1,861	3,943	4,840	3,029	37	30	1,857
		Median	-	-	98	69	4,805	0.04	73	1.6	27	18	3.6	0.49	9
		Mean	-	-	5,792	185	5,286	3.5	191	160	383	88	5.5	1.8	95
		IQR	-	-	10,585-10	296-15	7,824-1,103	0.47-0.01	164-36	27-0.22	114-4.53	68-6	4.9-2.6	1.3-0.14	68-2
San Vicente deposit	All analyses (n = 155)	MIN.	61.7	B.D.L.	B.D.L.	3.0	185	B.D.L.	B.D.L.	0.038	B.D.L.	1.8	1.9	B.D.L.	3
		MAX.	67.9	4.7	43,271	1,161	9,924	18	1,861	997	2,084	3,029	9.1	25	439
		Median	65.4	2.0	12,463	45	861	0.02	68	2.2	4	8.8	3.6	0.9	10
		Mean	65.3	1.6	13,061	122	1,778	0.8	148	27	92	117	4.0	2.1	34
		IQR	66.4-64.3	2.4-0.6	19,577-5,479	97-23	1,974-535	0.14-0.008	118-44	13-0.25	7-4	44,699	4.4-3.2	2.5-0.49	21-5
	sl₁ (n = 118)	MIN.	61.7	0.25	3,000	3.0	185	B.D.L.	13	0.038	B.D.L.	2	1.9	0.036	3
		MAX.	67.5	4.7	43,271	172	3,784	0.65	180	80	10	38	8.6	7.0	439
		Median	64.8	2.0	16,674	32	714	0.01	61	1.0	4	6	3.4	0.9	12
		Mean	65.0	2.0	17,038	39	840	0.039	71	4.4	4	9	3.5	1.4	41
		IQR	66.4-64.3	2.4-0.7	20,663-10,680	52-21	1,080-489	0.04-0.01	91-44	4.4-0.18	44,656	11-4	3.9-3.1	1.6-0.52	27-6
	sl_{1bl} (n = 34)	MIN.	61.7	0.3	9,774	7.4	311	B.D.L.	19	0.064	B.D.L.	2	2.4	0.26	3
		MAX.	67.5	4.7	43,271	172	3,784	0.65	180	80	8	29	8.6	3.2	167
		Median	64.5	2.0	20,525	43	591	0.018	72	3.0	4	6.0	3.4	0.9	12
		Mean	64.6	2.2	22,066	47	762	0.067	79	7.0	5	9	3.7	1.1	21
		IQR	65.9-63.8	2.4-1.5	25,831-16,671	63-25	899-495	0.06-0.01	105-54	7.1-0.23	44,657	2-4	4.0-2.9	1.2-0.66	22-6
	sl_{1rb} (n = 27)	MIN.	62.2	0.6	8,342	8.9	185	B.D.L.	31	0.038	B.D.L.	2	1.9	0.23	3
		MAX.	67.1	4.2	32,945	77	1,430	0.21	168	48	8	21	5.4	3.1	183
		Median	64.4	2.4	19,687	35	746	0.010	54	0.136	4	5	3.2	0.6	14
		Mean	64.6	2.3	19,531	39	727	0.028	71	3.4	4	6	3.2	0.91	26
IQR		65.4-63.9	2.7-1.5	22,035-15,116	54-23	897-503	0.02-0.007	90-43	2.8-0.07	5-4	6-3	3.5-2.4	1.3-0.41	23-9	
sl_{1yb} (n = 45)	MIN.	63.1	0.4	3,000	3.0	247	B.D.L.	13	0.044	B.D.L.	2	2.0	0.036	3	
	MAX.	67.3	3.6	38,867	97	2,458	0.23	167	26	10	38	5.7	7.0	439	
	Median	65.1	1.9	12,906	37	786	0.012	55	1.2	3.8	7	3.5	0.9	8.8	
	Mean	65.0	1.8	13,278	38	912	0.030	63	3.4	4.1	9	3.5	1.6	54	
	IQR	65.5-64.3	2.4-1.2	16,839-9,473	47-18	1,447-456	0.04-0.008	83-42	3.2-0.47	4-3.5	10-5	3.9-3.2	2.5-0.43	38-5	
sl_{1y} (n = 12)	MIN.	63.8	1.2	6,309	6.3	531	B.D.L.	37	0.049	B.D.L.	3	2.1	0.34	3	
	MAX.	65.9	2.4	16,235	68	1,598	0.067	144	17	5	22	5.7	4.3	237	
	Median	65.2	1.8	11,562	17	958	0.008	60	0.23	4	15	3.6	2.2	58	
	Mean	65.1	1.8	11,281	20	1,039	0.016	78	2.5	4	14	3.7	2.1	79	
	IQR	65.4-64.9	2.0-1.5	13,656-8,621	23-11	1,383-731	0.01-0.006	104-46	1.3-0.16	5-3	20-7	4.3-3.1	2.9-1.3	145-8	
sl₂ (n = 37)	MIN.	65.6	B.D.L.	B.D.L.	139	1,363	B.D.L.	B.D.L.	0.21	B.D.L.	6	3.5	B.D.L.	3.0	
	MAX.	67.9	B.D.L.	122	1,161	9,924	18	1,861	997	2,084	3,029	9.1	25	173	
	Median	66.6	-	14	338	4,356	1.2	177	47	104	33	5.2	3.7	4	
	Mean	66.5	-	28	391	4,772	3.3	392	100	381	463	5.6	4.3	15	
	IQR	66.3-64.3	-	30-11	471-261	5,704-3,440	4.5-0.39	566-41	93-14.9	461-17	627-15	6.2-4.5	7.4-0.25	9-4	
sl_{2o} (n = 13)	MIN.	66.2	B.D.L.	B.D.L.	139	3,489	0.0084	0.18	0.21	55	15	4.0	0.0093	4	
	MAX.	67.6	B.D.L.	17	683	8,253	18	1,861	997	2,084	3,029	9.1	9.6	173	
	Median	66.7	-	11	340	5,126	3.7	621	64	633	627	5.3	3.6	8	
	Mean	66.8	-	11	379	5,577	5.9	747	172	890	990	5.5	3.6	27	
	IQR	67.0-66.6	-	12-10	524-266	7,180-4,281	8.2-2.2	1,207-375	200-11.6	1,446-392	1,335-414	5.8-4.5	5.4-0.22	18-6	
sl_{2y} (n = 19)	MIN.	65.8	B.D.L.	B.D.L.	146	1,363	B.D.L.	6.7	0.76	B.D.L.	5.8	3.5	0.020	3	
	MAX.	67.9	B.D.L.	122	1,161	9,924	8.6	1,096	306	1,149	1,959	7.3	25	82	
	Median	66.1	-	29	314	3,440	0.5	176	25	18	20	4.8	5.1	4	
	Mean	66.3	-	43	392	4,308	1.1	252	43	125	217	4.9	5.9	9	
	IQR	66.7-65.8	-	62-15	375-244	5,307-3,120	0.93-0.18	269-130	49-15	80-4	69-13	5.2-4.4	8.1-1.9	5.1-3.4	
	MIN.	67.4	B.D.L.	B.D.L.	273	3,817	3.8	B.D.L.	92	96	14	8.3	B.D.L.	4	
	MAX.	67.4	B.D.L.	13	593	4,805	5.8	2.1	195	206	46	8.9	0.15	5	

Ore-body/vein	Sphalerite type		Zn (wt%)	Fe (wt%)	Fe (ppm)	Mn (ppm)	Cd (ppm)	In (ppm)	Ge (ppm)	Ga (ppm)	Cu (ppm)	Ag (ppm)	Hg (ppm)	Tl (ppm)	As (ppm)	
Chilpes prospect	sl _{2w} (n = 5)	Median	67.4	-	11	382	4,497	4.5	0.16	99	112	27	8.5	0.01	4	
		Mean	67.4	-	12	423	4,441	4.6	0.54	130	137	28	8.5	0.04	4	
		IQR	-	-	12-11	486-381	4,727-4,356	5.0-3.9	0.23-0.14	171-93	172-96	30-22	8.5-8.4	0-0.01	4.0-3.8	
	All analyses (n = 175)	MIN.	n.a.	n.a.	B.D.L.	B.D.L.	4,024	B.D.L.	B.D.L.	B.D.L.	B.D.L.	B.D.L.	1	1.3	B.D.L.	0.06
		MAX.	n.a.	n.a.	187	803	16,422	92	1,745	3,943	4,840	347	37	37	11	1,857
		Median	n.a.	n.a.	10	138	7,545	0.04	92	0.8	88	42	2.9	0.20	5	
		Mean	n.a.	n.a.	54	211	8,070	6.3	208	292	694	59	7.0	0.51	133	
		IQR	n.a.	n.a.	98-9	433-1.6	10,103-4,965	0.33-0.011	193-20	22-0.2	392-38	85-11	7.7-2.1	0.4-0.07	100-0.8	
	sl _{rb} (n = 66)	MIN.	n.a.	n.a.	B.D.L.	129	4,139	B.D.L.	B.D.L.	B.D.L.	5	2	1.5	0.020	0.17	
		MAX.	n.a.	n.a.	13	716	10,310	92	1,745	3,943	4,840	347	37	2.4	1,857	
		Median	n.a.	n.a.	9	502	6,130	0.41	131	33	1,318	48	10	0.26	135	
		Mean	n.a.	n.a.	9.3	452	6,496	16	383	759	1,686	63	13	0.40	329	
	sl _{yb} (n = 27)	IQR	n.a.	n.a.	9.4-9.0	623-254	7,823-4,857	26-0.021	445-22	1,156-0.3	2,866-159	95-11	21-4.5	0.5-0.07	480-60	
		MIN.	n.a.	n.a.	B.D.L.	122	4,024	B.D.L.	B.D.L.	0.040	B.D.L.	1	1.4	B.D.L.	0.10	
		MAX.	n.a.	n.a.	10	438	7,071	3.0	736	139	1,495	52	25	0.21	386	
		Median	n.a.	n.a.	9	144	4,422	0.03	7.3	1.4	44	4	2.0	0.05	24	
	sl _y (n = 16)	Mean	n.a.	n.a.	9	183	4,633	0.27	58	16	151	7	3.7	0.061	53	
		IQR	n.a.	n.a.	9.5-9.0	195-139	4,682-4,290	0.18-0.011	11-5	11-0.9	82-27	6-2	3.5-1.7	0.1-0.04	54-6.4	
		MIN.	n.a.	n.a.	74	B.D.L.	5,115	0.006	18	0.068	17	12	1.3	0.031	0.09	
		MAX.	n.a.	n.a.	127	247	14,033	0.48	283	27	279	257	8.2	11	54	
	sl _y (n = 66)	Median	n.a.	n.a.	94	5.8	8,276	0.02	129	0.4	122	80	2.5	0.4	0.8	
Mean		n.a.	n.a.	97	26	8,972	0.095	134	2.9	126	95	3.0	2.2	10		
IQR		n.a.	n.a.	102-87	13-1.6	11,266-6,621	0.09-0.012	172-96	0.7-0.2	162-86	121-58	3.3-2.1	1.6-0.19	7-0.59		
MIN.		n.a.	n.a.	B.D.L.	B.D.L.	4,530	B.D.L.	0.31	B.D.L.	5	2	1.9	0.01	0.06		
Huacrash prospect	sl _{bo} (n = 27)	MAX.	n.a.	n.a.	187	803	16,422	0.57	293	129	251	317	13	2.4	11	
		Median	n.a.	n.a.	104	1.4	11,028	0.025	101	0.2	51	45	2.5	0.3	0.82	
		Mean	n.a.	n.a.	108	26	10,833	0.066	112	6.6	63	68	3.1	0.38	0.74	
		IQR	n.a.	n.a.	128-93	2.3-1.4	13,335-8,977	0.06-0.009	164-55	1.4-0.1	83-27	90-31	3.3-2.2	0.5-0.11	0.9-0.13	
		MIN.	n.a.	n.a.	B.D.L.	114	3,491	0.37	10	4.1	10	14	3.9	0.56	1.0	
	All analyses (n = 50)	MAX.	n.a.	n.a.	6,934	722	8,200	3.6	855	107	37	330	5.0	30	1,126	
		Median	n.a.	n.a.	21	307	7,713	1.5	205	61	17	84	4.2	10	35	
		Mean	n.a.	n.a.	1,514	369	7,381	1.8	327	65	22	110	4.3	8.7	184	
		IQR	n.a.	n.a.	2,597-8	505-279	7,970-7,403	2.6-1.0	650-34	97-50	31-15	188-27	4.4-4.0	15-0.85	291-3	
		MIN.	n.a.	n.a.	B.D.L.	181	B.D.L.	1,501	B.D.L.	2.7	B.D.L.	B.D.L.	6	3.0	0.011	4
Shalipayco deposit	All analyses (n = 50)	MAX.	n.a.	n.a.	37,888	14	7,687	2.6	1,119	32	5,090	1,600	780	6.7	93	
		Median	n.a.	n.a.	1,017	1.4	3,808	0.01	299	0.4	5	270	115	1.1	13	
		Mean	n.a.	n.a.	4,893	3.2	3,898	0.11	316	4.4	239	362	203	1.6	20	
		IQR	n.a.	n.a.	2,793-666	3.4-1.1	4,487-2,741	0.01-0.007	425-101	2.8-0.08	131-4	508-56	313-58	1.9-0.44	22-8	
	sl _{rb} (n = 13)	MIN.	n.a.	n.a.	384	B.D.L.	1,501	B.D.L.	4.5	0.032	B.D.L.	12	8.7	0.037	4	
		MAX.	n.a.	n.a.	37,888	14	7,687	1.1	731	1.3	5,090	512	780	6.7	62	
		Median	n.a.	n.a.	3,116	1.4	4,032	0.01	249	0.2	4	163	408	1.5	10	
		Mean	n.a.	n.a.	11,193	5.2	3,943	0.10	254	0.5	429	192	315	2.0	18	
	sl _{yb} (n = 30)	IQR	n.a.	n.a.	18,937-820	7.8-1.1	4,936-2,295	0.01-0.006	384-52	1-0.1	4.0-3.9	320-26	451-50	2.2-0.98	20-7	
		MIN.	n.a.	n.a.	181	B.D.L.	2,425	B.D.L.	2.7	B.D.L.	B.D.L.	6	3.0	0.011	5	
MAX.		n.a.	n.a.	22,783	7.9	7,048	2.6	966	32	1,347	1,600	772	5.5	93		
Median		n.a.	n.a.	1,040	1.5	3,871	0.01	307	0.5	11	295	119	0.8	15		
sl _y (n = 7)	Mean	n.a.	n.a.	3,151	2.7	4,094	0.11	321	4.5	183	389	180	1.4	23		
	IQR	n.a.	n.a.	1760-786	3.2-1.2	4,639-3,396	0.01-0.007	468-71	3-0.1	183-4.5	511-63	272-75	1.6-0.25	26-8		
	MIN.	n.a.	n.a.	424	B.D.L.	2,134	B.D.L.	156	0.073	B.D.L.	176	45	0.34	7		
	MAX.	n.a.	n.a.	882	3.2	4,058	0.57	1,119	31	549	1,469	301	3.8	14		
sl _y (n = 7)	Median	n.a.	n.a.	666	1.1	3,010	0.01	304	3.1	31	540	57	0.6	8		
	Mean	n.a.	n.a.	659	1.47	2,977	0.12	409	11	128	562	95	1.4	9		

Ore-body/vein	Sphalerite type	Zn (wt%)	Fe (wt%)	Fe (ppm)	Mn (ppm)	Cd (ppm)	In (ppm)	Ge (ppm)	Ga (ppm)	Cu (ppm)	Ag (ppm)	Hg (ppm)	Tl (ppm)	As (ppm)	
		IQR	n.a.	n.a.	746-573	1.4-1.1	3,474-2,343	0.13-0.01	375-267	21-0.2	152-5	574-300	81-50	1.9-0.52	10-8
Cristal (n = 20; Mondillo et al. 2018b)		MIN.	54.4	5.3	n.a.	7.6	1,939	B.D.L.	0.25	B.D.L.	40	1	n.a.	n.a.	n.a.
		MAX.	61.9	12.9	n.a.	40	8,429	37	386	6.6	229	134	n.a.	n.a.	n.a.
		Median	59.1	8.0	n.a.	17	4,923	0.13	131	0.1	80	12	n.a.	n.a.	n.a.
		Mean	58.2	8.2	n.a.	19	4,600	3.2	142	1.3	112	38	n.a.	n.a.	n.a.
		IQR	59.9-56.3	10.0-6.2	n.a.	26-9	5,867-2,562	0.51-0.010	231-31	1.8-0.05	182-53	77-3	n.a.	n.a.	n.a.

EMPA data in wt.%. LA-ICP-MS data in ppm.

n refers to the number of LA-ICP-MS analyses

B.D.L.: below detection limit; n.a.: not analyzed

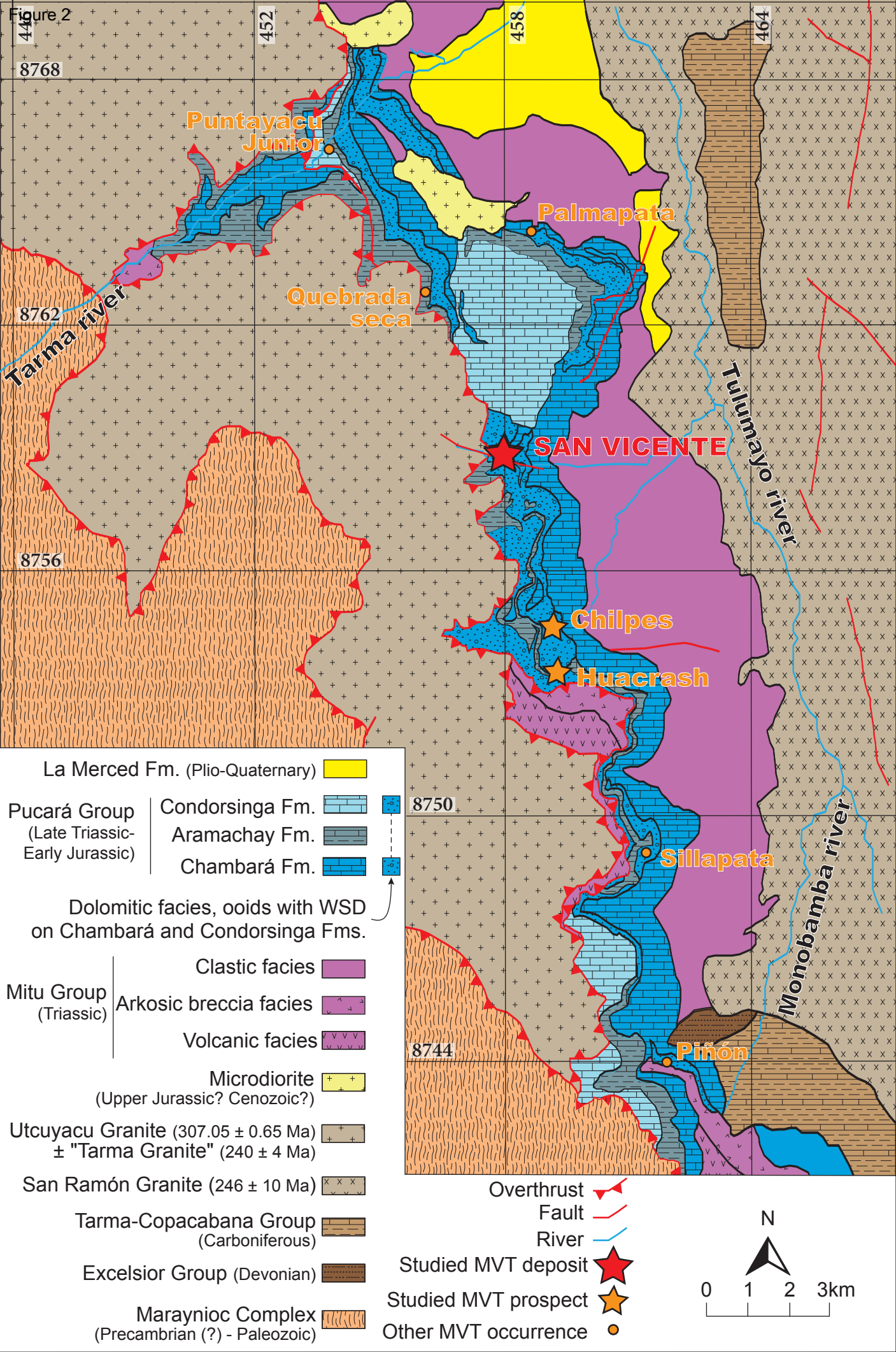
For values B.D.L., individual detection limits as shown in ESM Table S4 have been taken into account for the calculation of median, average, and IQR values.

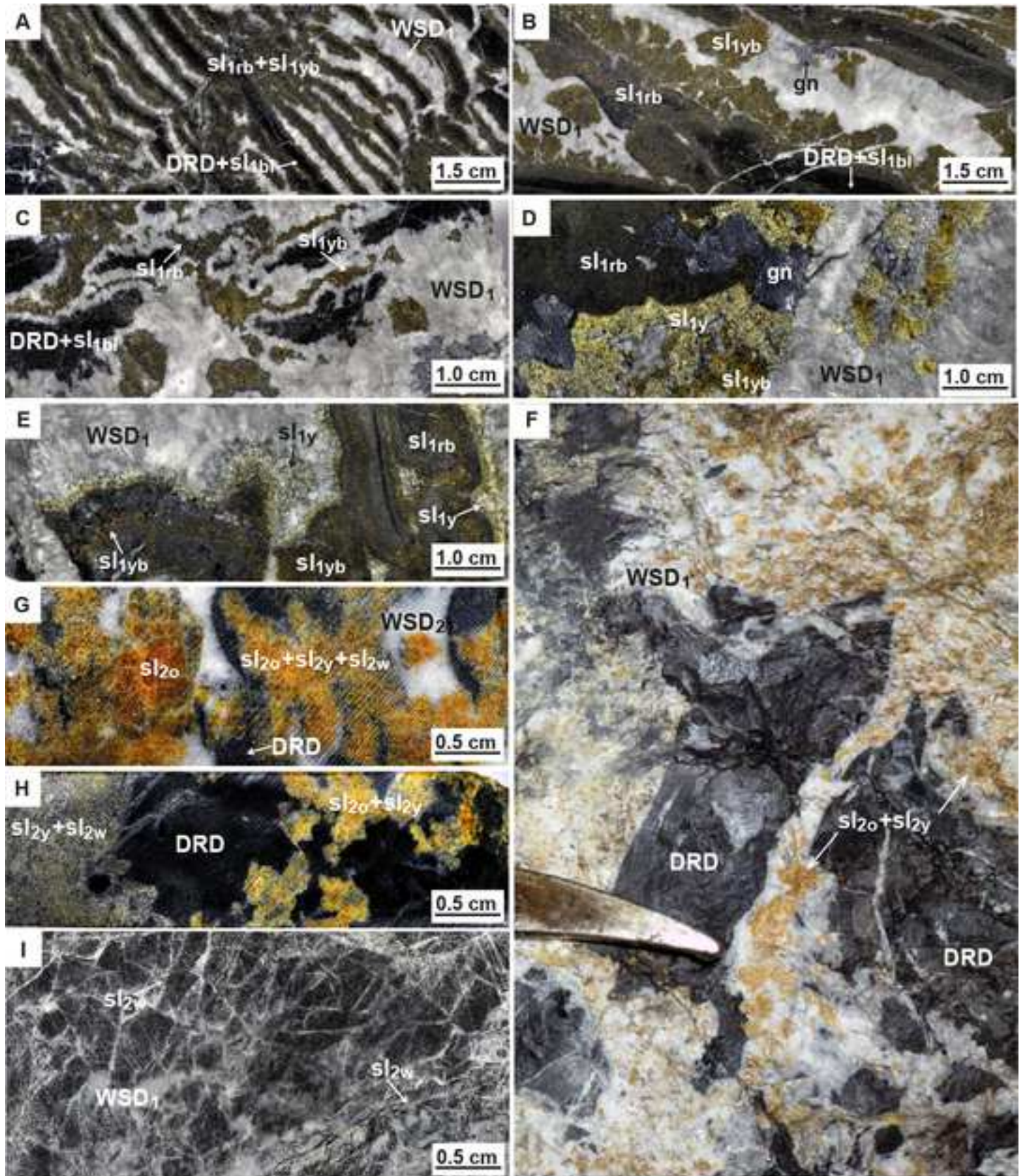
Table 2

Ore-body/vein	Sphalerite type	n	Median	Mean	2 sigma
San Vicente deposit	sl _{1bl}	33	181	183	41
	sl _{1rb}	27	200	195	43
	sl _{1yb}	45	174	174	46
	sl _{1y}	12	168	171	54
	sl _{2o}	12	29	28	60
	sl _{2y}	18	56	51	31
Chilpes prospect	sl _{rb}	66	35	39	100
	sl _{yb}	27	70	71	68
	sl _o	16	65	67	53
	sl _y	66	63	61	49
Huacrash prospect	sl _{bo}	27	59	82	105
Shalipayco deposit	sl _{rb}	12	142	136	101
	sl _{yb}	30	83	98	113
	sl _y	7	54	58	37
Cristal (Mondillo et al. 2018b)		15	218	234	77

Figure 1







San Vicente deposit

1st step

2nd step

San Vicente deposit		1 st step	2 nd step
Dolomite	$\text{CaMg}(\text{CO}_3)_2$	— <i>DRD</i> <i>WSD</i> ₁ —	— <i>WSD</i> ₂
Quartz	SiO_2	- - - -	
Pyrite	FeS_2	- - - - -	- - - - -
Marcasite		- - - - -	- - - - -
Sphalerite 1	ZnS	<i>sl</i> _{1bl} —	
		<i>sl</i> _{1rb} —	
		<i>sl</i> _{1yb} —	
		<i>sl</i> _{1y} —	
Sphalerite 2			<i>sl</i> _{2o} —
			<i>sl</i> _{2y} —
			<i>sl</i> _{2w} —
Galena	PbS	- - - - -	- - - - -
Gratonite	$\text{Pb}_9\text{As}_4\text{S}_{15}$	- -	
Calcite	CaCO_3	- - -	- - - - -

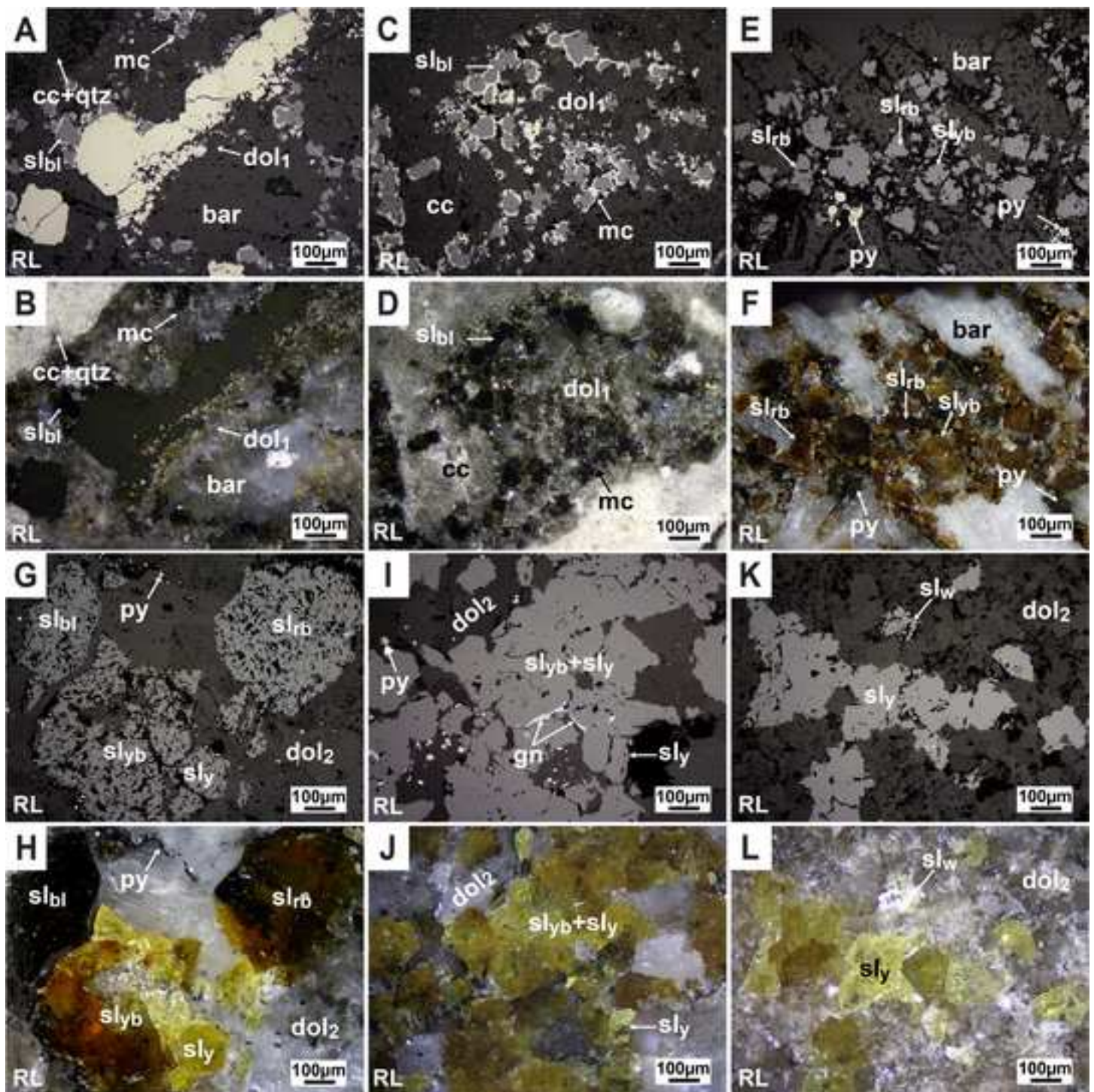
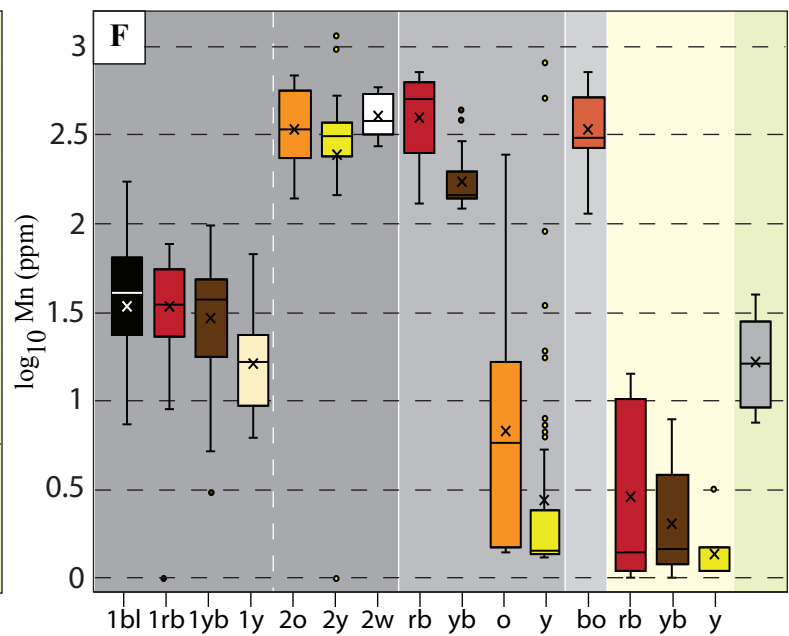
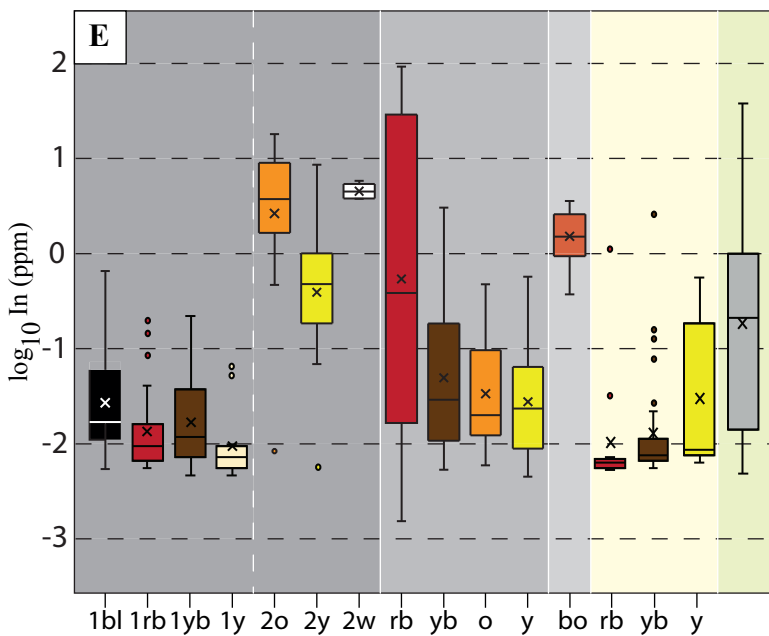
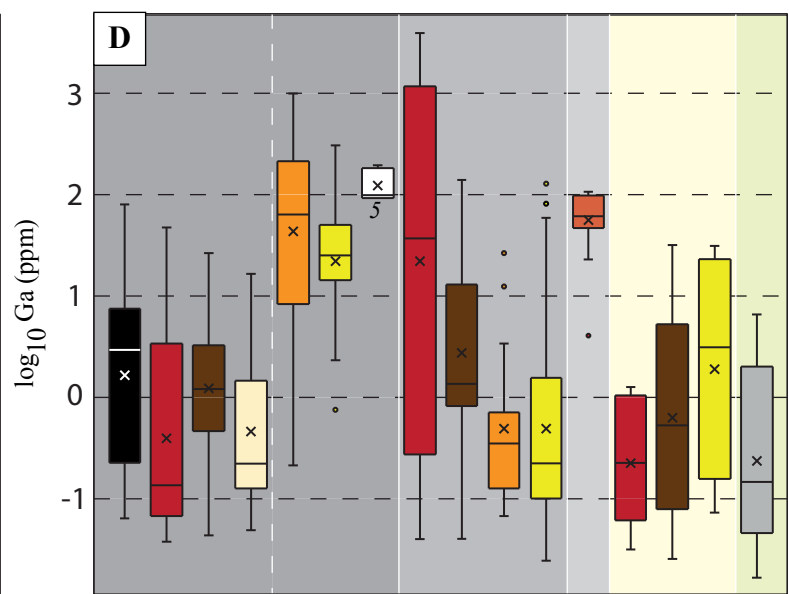
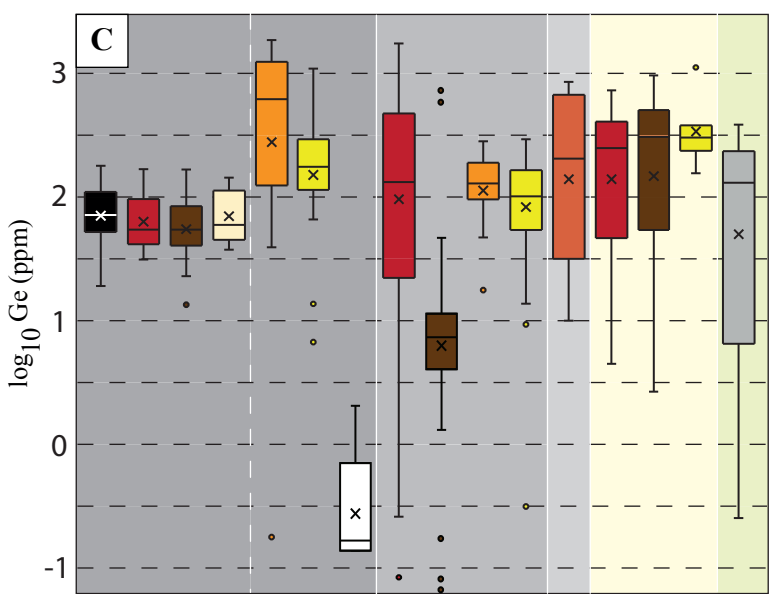
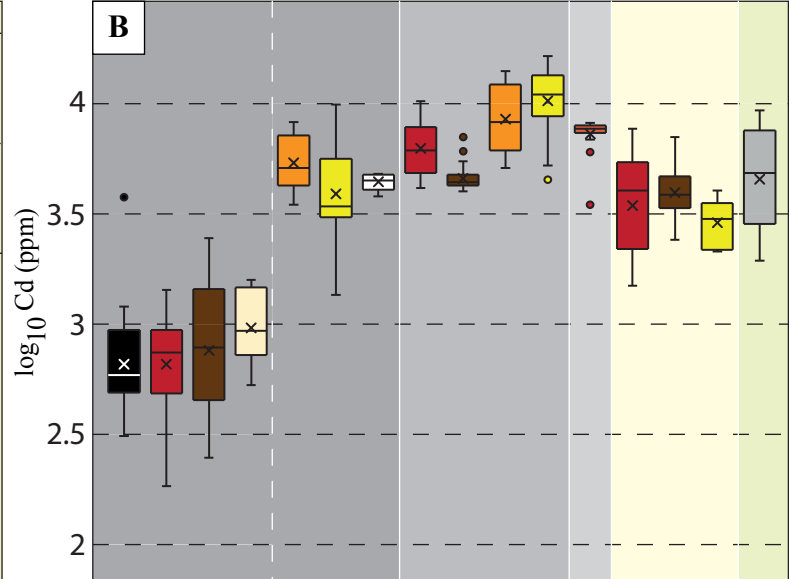
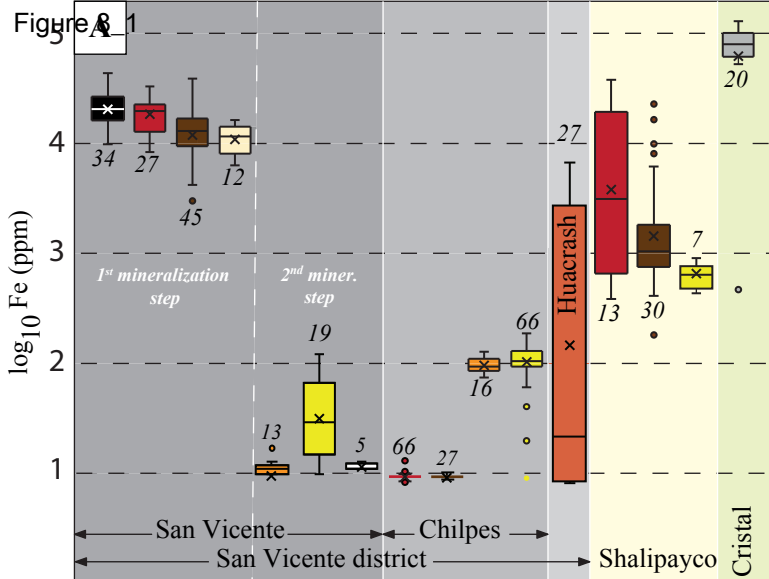
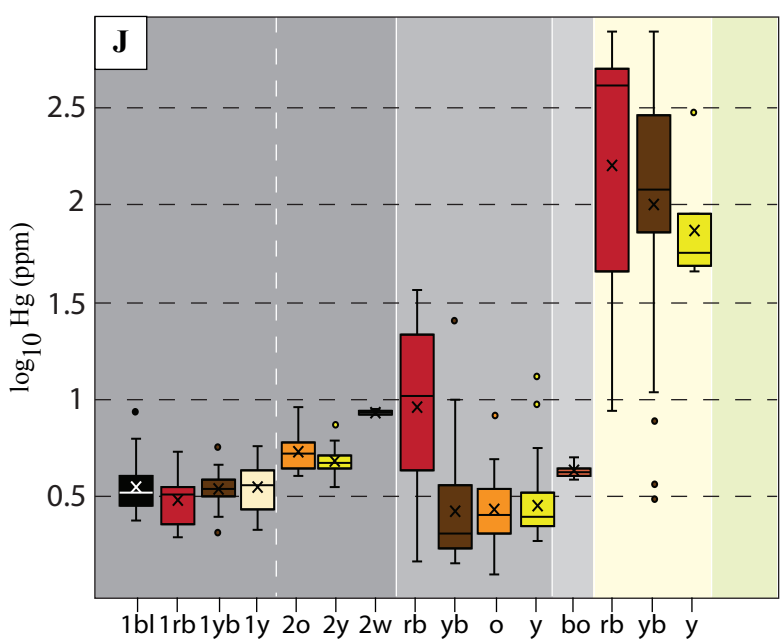
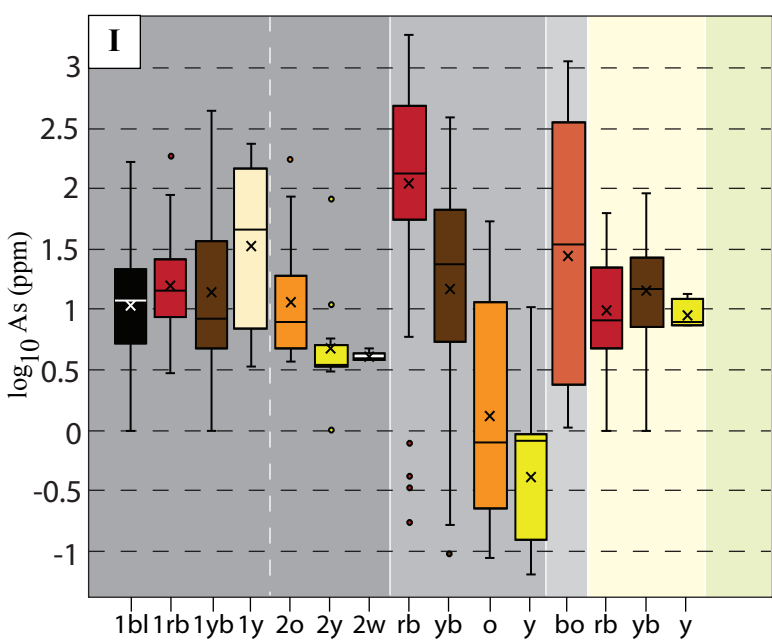
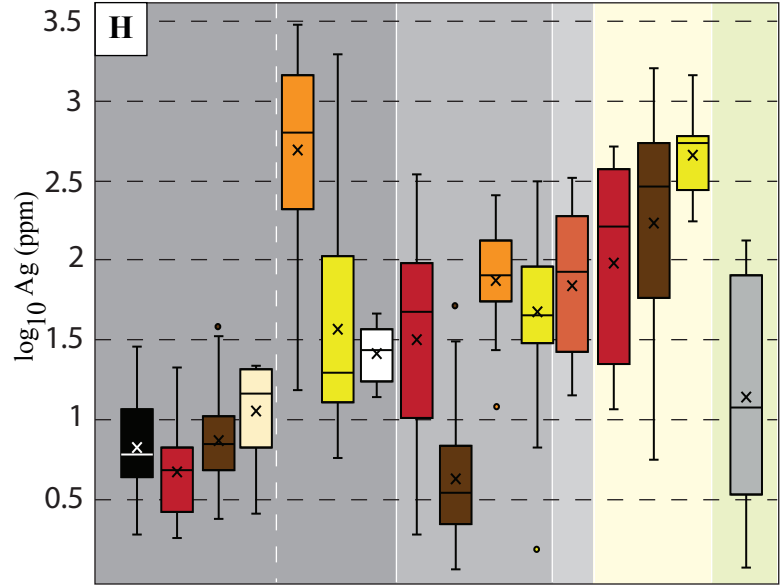
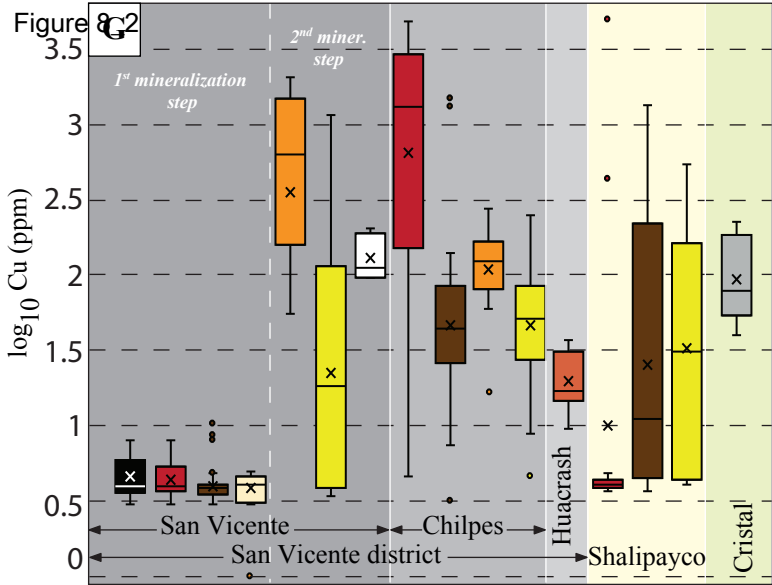


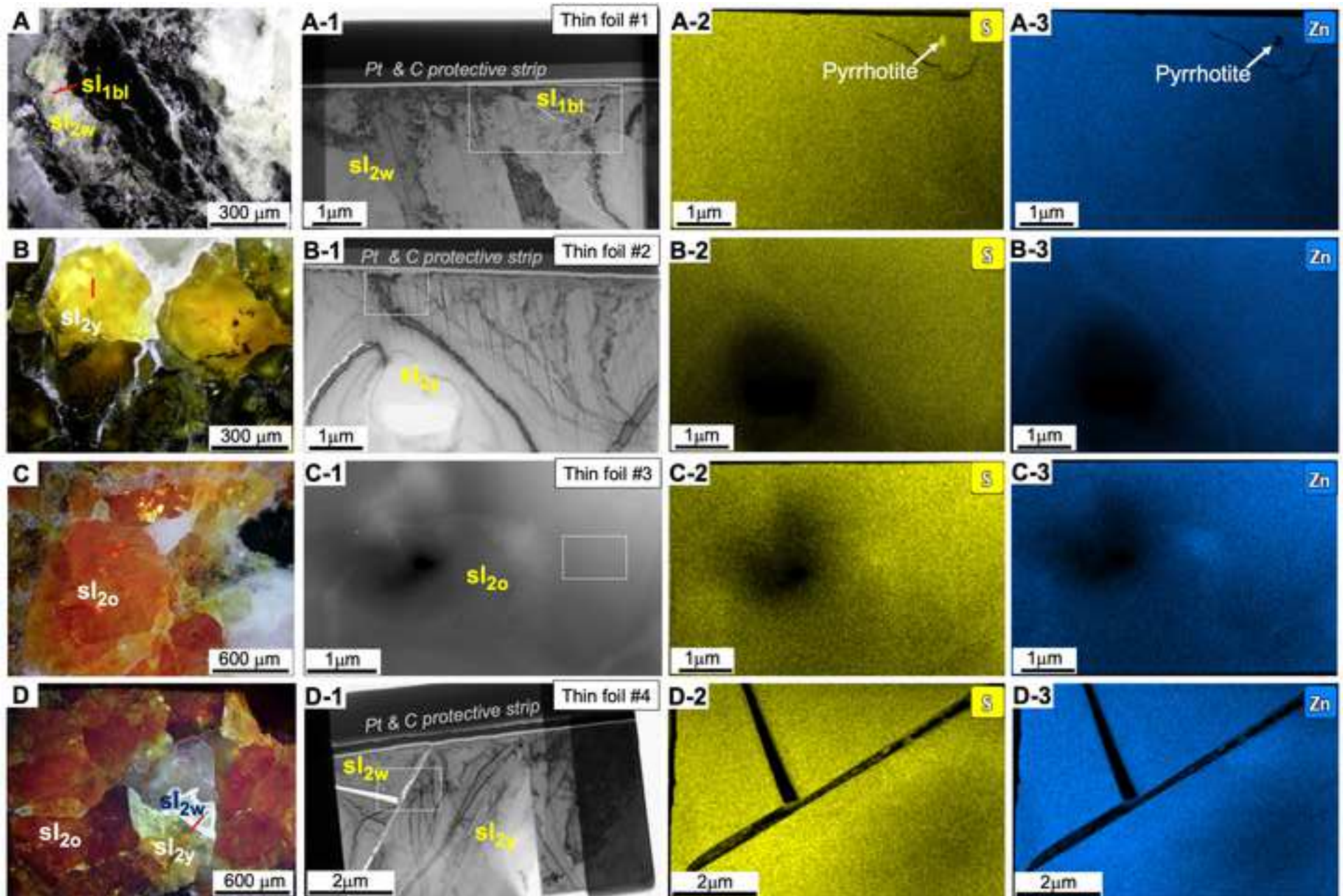
Figure 7

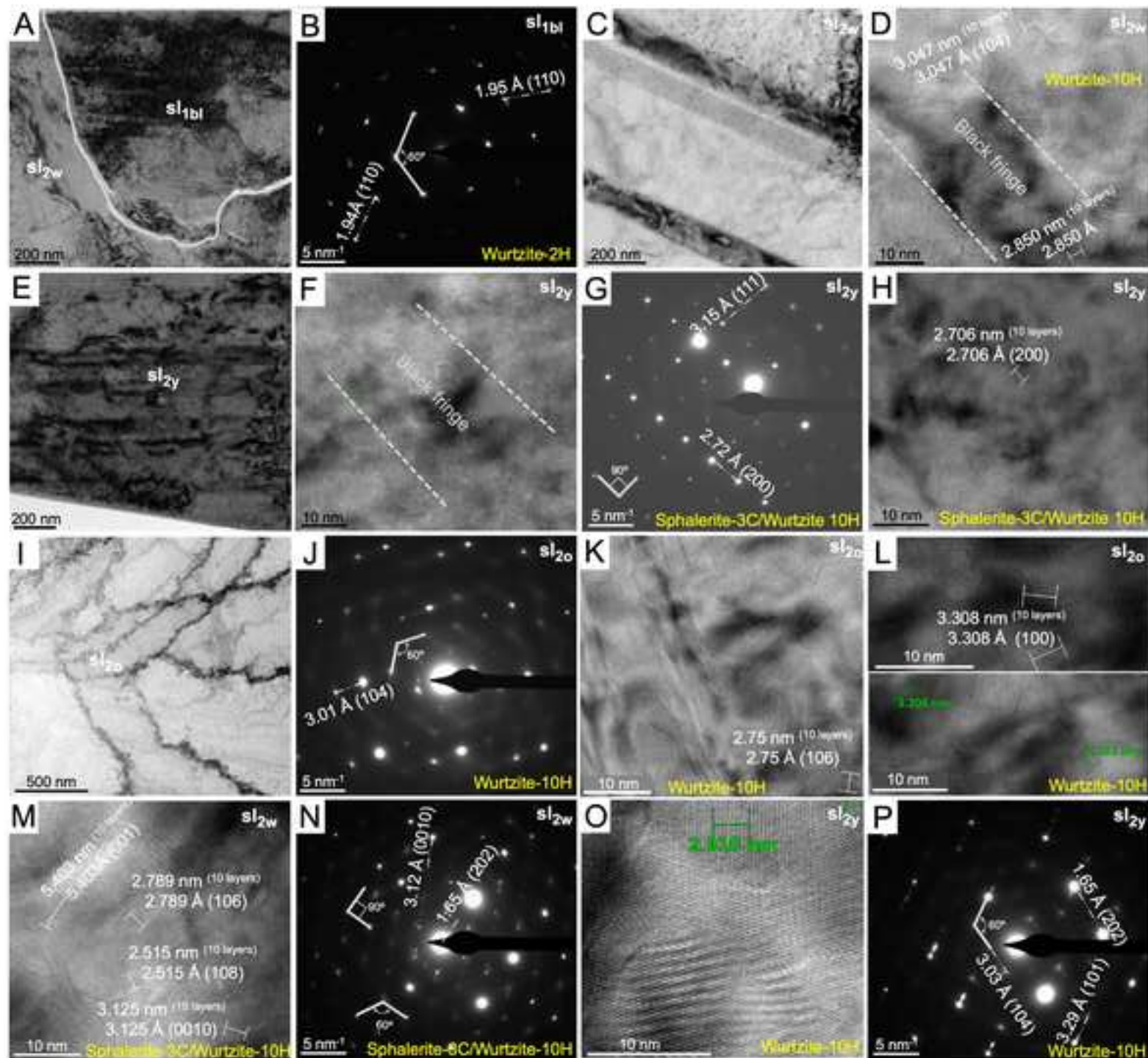
Shalipayco deposit

Quartz	SiO_2	—
Dolomite	$\text{CaMg}(\text{CO}_3)_2$	-----dol ₁ dol ₂ -----
Pyrite	FeS_2	-----
Sphalerite	ZnS	sl _{bl} —
		sl _{rb} —
		sl _{yb} —
		sl _y —
		sl _w —
Marcasite	FeS_2	-----
Galena	PbS	—
Baryte	BaSO_4	—
Calcite	CaCO_3	—









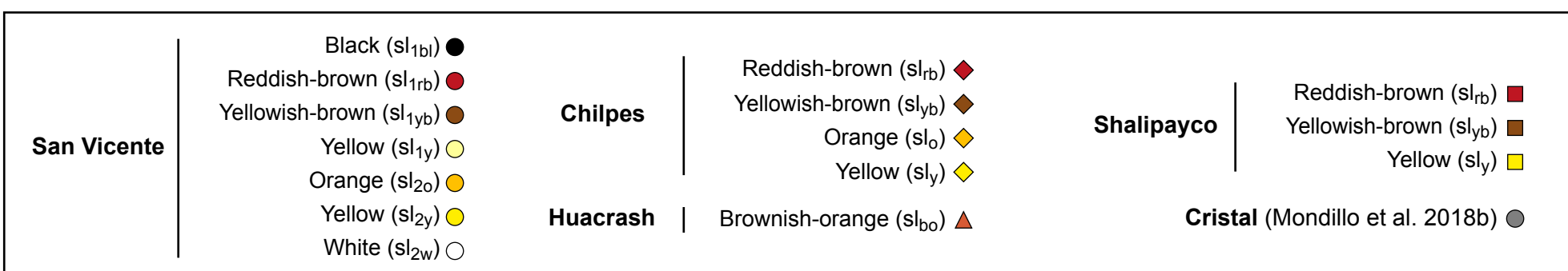
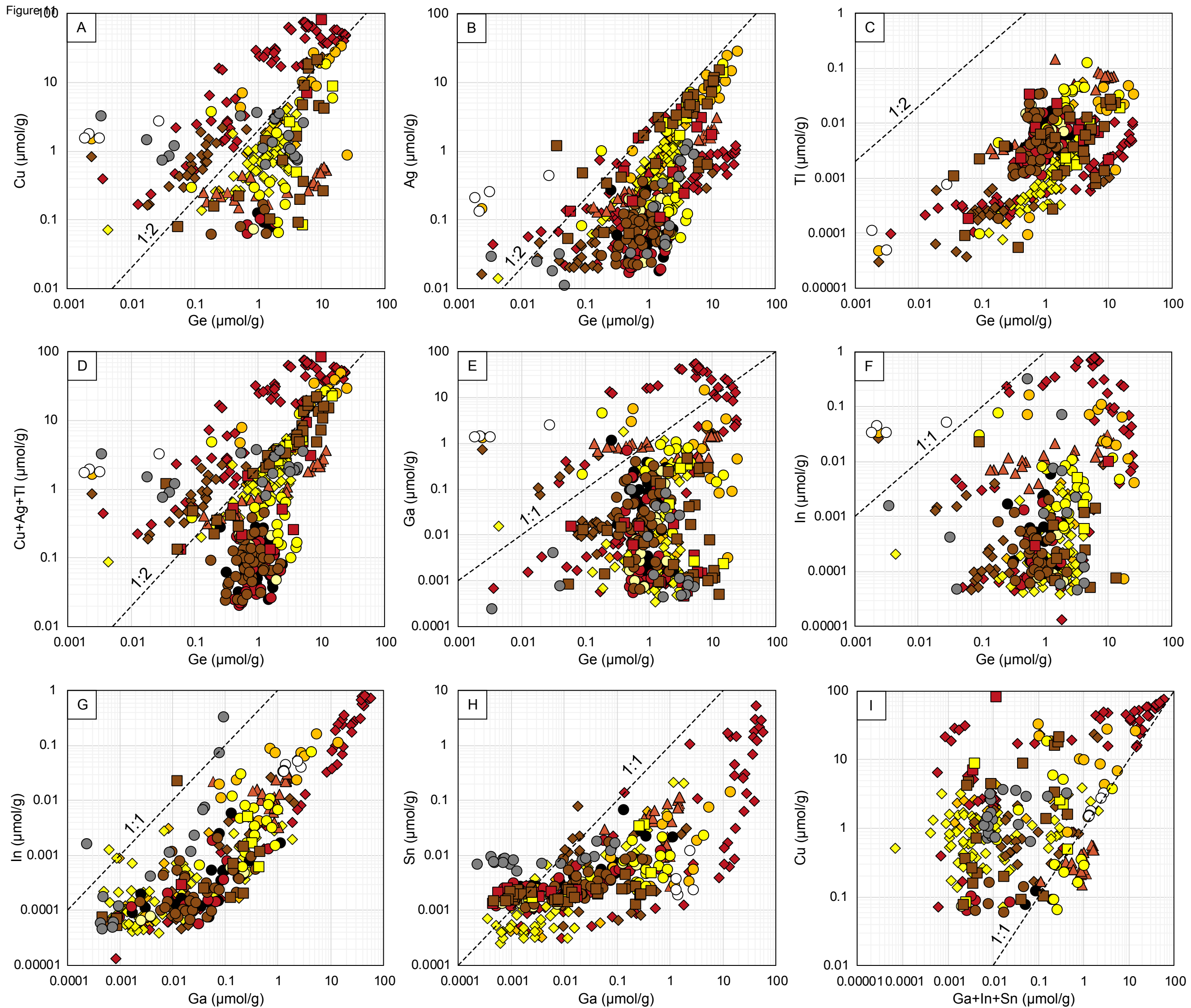


Figure 12

